



Study of 72 Pulsars Discovered in the PALFA Survey: Timing Analysis, Glitch Activity, Emission Variability, and a Pulsar in an Eccentric Binary

E. Parent¹, H. Sewalls¹, P. C. C. Freire², T. Matheny^{3,4}, A. G. Lyne⁵, B. B. P. Perera⁶, F. Cardoso^{3,4}, M. A. McLaughlin^{3,4}, B. Allen^{7,8}, A. Brazier⁹, F. Camilo¹⁰, S. Chatterjee⁹, J. M. Cordes⁹, F. Crawford¹¹, J. S. Deneva¹², F. A. Dong¹³, R. D. Ferdman¹⁴, E. Fonseca^{1,3,4}, J. W. T. Hessels^{15,16}, V. M. Kaspi¹, B. Knispel⁷, J. van Leeuwen^{15,16}, R. S. Lynch¹⁷, B. M. Meyers¹³, J. W. McKee¹⁸, M. B. Mickaliger⁵, C. Patel^{1,19}, S. M. Ransom²⁰, A. Rochon¹, P. Scholz¹⁹, I. H. Stairs¹³, B. W. Stappers⁵, C. M. Tan¹, and W. W. Zhu²¹

¹Dept. of Physics and McGill Space Institute, McGill Univ., Montreal, QC H3A 2T8, Canada; parente@physics.mcgill.ca

²Max-Planck-Institut für Radioastronomie, Auf dem Hügel 69, Bonn D-53121, Germany

³Department of Physics and Astronomy, West Virginia University, Morgantown, WV 26506-6315, USA

⁴Center for Gravitational Waves and Cosmology, Chestnut Ridge Research Building, Morgantown, WV 26505, USA

⁵Jodrell Bank Centre for Astrophysics, School of Physics and Astronomy, University of Manchester, Manchester, M13 9PL, UK

⁶Arecibo Observatory, HC3 Box 53995, Arecibo, PR 00612, USA

⁷Max-Planck-Institut für Gravitationsphysik (Albert-Einstein-Institut), D-30167 Hannover, Germany

⁸Department of Physics, University of Wisconsin—Milwaukee, Milwaukee WI 53211, USA

⁹Cornell Center for Astrophysics and Planetary Science, Ithaca, NY 14853, USA

¹⁰South African Radio Astronomy Observatory, Observatory, 7925, South Africa

¹¹Department of Physics and Astronomy, Franklin and Marshall College, Lancaster, PA 17604-3003, USA

¹²George Mason University, Resident at the Naval Research Laboratory, Washington, DC 20375, USA

¹³Dept. of Physics and Astronomy, University of British Columbia, 6224 Agricultural Road, Vancouver, BC V6T 1Z1, Canada

¹⁴School of Chemistry, University of East Anglia, Norwich Research Park, Norwich, NR4 7TJ, UK

¹⁵ASTRON, the Netherlands Institute for Radio Astronomy, Oude Hoogeveensedijk 4, 7991 PD Dwingeloo, The Netherlands

¹⁶Anton Pannekoek Institute for Astronomy, University of Amsterdam, Postbus 94249, 1090 GE Amsterdam, The Netherlands

¹⁷Green Bank Observatory, P.O. Box 2, Green Bank, WV 24494, USA

¹⁸Canadian Institute for Theoretical Astrophysics, University of Toronto, 60 Saint George Street, Toronto, ON M5S 3H8, Canada

¹⁹Dunlap Institute for Astronomy & Astrophysics, University of Toronto, 50 St. George Street, Toronto, ON M5S 3H4, Canada

²⁰National Radio Astronomy Observatory, 520 Edgemont Rd., Charlottesville, VA 22903, USA

²¹CAS Key Laboratory of FAST, NAOC, Chinese Academy of Sciences, Beijing 100101, People's Republic of China

Received 2021 August 4; revised 2021 November 3; accepted 2021 November 3; published 2022 January 19

Abstract

We present new discoveries and results from long-term timing of 72 pulsars discovered in the Pulsar Arecibo *L*-band Feed Array (PALFA) survey, including precise determination of astrometric and spin parameters, and flux density and scatter broadening measurements at 1.4 GHz. Notable discoveries include two young pulsars (characteristic ages ~ 30 kyr) with no apparent supernova remnant associations, three mode-changing, 12 nulling and two intermittent pulsars. We detected eight glitches in five pulsars. Among them is PSR J1939+2609, an apparently old pulsar (characteristic age ~ 1 Gy), and PSR J1954+2529, which likely belongs to a newly emerging class of binary pulsars. The latter is the only pulsar among the 72 that is clearly not isolated: a nonrecycled neutron star with a 931 ms spin period in an eccentric ($e = 0.114$) wide ($P_b = 82.7$ days) orbit with a companion of undetermined nature having a minimum mass of $\sim 0.6 M_\odot$. Since operations at Arecibo ceased in 2020 August, we give a final tally of PALFA sky coverage, and compare its 207 pulsar discoveries to the known population. On average, they are 50% more distant than other Galactic plane radio pulsars; PALFA millisecond pulsars (MSPs) have twice the dispersion measure per unit spin period than the known population of MSP in the plane. The four intermittent pulsars discovered by PALFA more than double the population of such objects, which should help to improve our understanding of pulsar magnetosphere physics. The statistics for these, rotating radio transients, and nulling pulsars suggest that there are many more of these objects in the Galaxy than was previously thought.

Key words: Radio pulsars – Pulsar timing method – Surveys – Binary pulsars – Radio transient sources

Supporting material: data behind figure

1. Introduction

The observed population of radio pulsars currently numbers over 3000.²² Approximately 500 of them have periods less than 100 ms, 80% of which are millisecond pulsars (MSPs) with

periods $\lesssim 30$ ms, whereas the other 20% are young or partially recycled neutron stars (NSs). The remaining objects are so-called “normal” pulsars. While discovering MSPs or partially recycled objects is important for fundamental physics experiments and NS mass measurements (e.g., Arzoumanian et al. 2018; Antoniadis et al. 2013; Martinez et al. 2015; Archibald et al. 2018; Fonseca et al. 2021) and studies of binary evolution (see recent review by D’Antona & Tailo 2020), expanding the known population of normal pulsars is essential for understanding the NS population in terms of birth rates, magnetic fields, spatial distribution, and similar statistics (e.g., Faucher-Giguère & Kaspi 2006), for probing the electron density (see

²² According to version 1.65 of the ATNF Catalog (Manchester et al. 2005), available here: www.atnf.csiro.au/research/pulsar/psrcat/.

review by Weisberg 1996) and magnetic fields (see review by Han 2017) of the interstellar medium (ISM), and to gain insight into pulsar-emission processes and associated plasma physics (see review by Cerutti & Beloborodov 2017).

The wealth of astrophysical studies emerging from pulsar astronomy is often made possible by long-term monitoring and timing of newly discovered sources. Pulsar timing builds upon their remarkable rotational stability and consists of developing a mathematical model that accurately and precisely predicts the time of a pulse emitted by a pulsar when detected on Earth. This leads directly to high-precision measurements of spin, astrometric, dispersion and (if applicable) binary parameters.

The Pulsar Arecibo *L*-band Feed Array (PALFA²³) was a Galactic plane survey for radio pulsars and fast transients conducted from 2004 to 2020 at 1.4 GHz with the Arecibo William E. Gordon 305 m telescope at the Arecibo observatory (AO) in Puerto Rico, USA. Extensive descriptions of the survey methodology can be found in the literature (e.g., Cordes et al. 2006; Swiggum et al. 2014; Lazarus et al. 2015; Parent et al. 2018; Patel et al. 2018). Thanks to Arecibo’s large collecting area and the high time and frequency resolution of PALFA data, the survey was particularly prolific in discovering highly dispersed MSPs (Champion et al. 2008; Deneva et al. 2012; Crawford et al. 2012; Allen et al. 2013; Scholz et al. 2015; Knispel et al. 2015; Stovall et al. 2016; Parent et al. 2019). It was also among the best surveys for finding compact binaries (Pol et al. 2021) and/or highly accelerated systems, as evidenced by the discovery of three compact double-neutron-star systems (DNSs): PSR J1906 +0746, the youngest DNS known (Lorimer et al. 2006a; van Leeuwen et al. 2015); PSR J1913+1102, a member of a new population of merging DNSs with large mass asymmetries (Lazarus et al. 2016; Ferdman et al. 2020); and PSR J1946 +2052, the most compact DNS known in the Galaxy (Stovall et al. 2018). PALFA was also the first pulsar survey to make use of volunteer distributed computing to search for compact binary systems (Allen et al. 2013), which is the most computationally intensive regions of parameter space. Besides MSPs, the survey found several rotating radio transients (RRATs; Deneva et al. 2009; Patel et al. 2018) and has significantly contributed to our understanding of fast radio bursts (FRBs) with the discovery of the first repeating FRB 121102 (Spitler et al. 2014, 2016; Scholz et al. 2016).

In total, the survey discovered 207 pulsars,²⁴ 46 of which are MSPs. PALFA has also discovered many slow pulsars: timing solutions for 66 of them were presented in Nice et al. (2013) and Lyne et al. (2017a, 2017b), with the latter describing two “intermittent” pulsars (Kramer et al. 2006) discovered in the survey.

In this work, we present the results of several years of follow-up timing observations of an additional 72 long-period (>100 ms) pulsars found by the PALFA survey. One pulsar, PSR J1930+1722, was codiscovered in 2013 by the Parkes Northern Galactic Plane survey (Lorimer et al. 2013). Of the 72 sources being studied here, 32 were presented in some of the aforementioned PALFA publications, but only basic parameters were provided, with no timing solutions reported for any of them. These are, together with their previous names, listed in Table 1. The remaining pulsars are new discoveries presented

here for the first time. In addition to these discoveries, we present a set of 23 new pulsars that are not studied in detail in this work; they are listed, with some basic parameters, in Table 2 and will be described in detail elsewhere.

In Section 2, we give an overview of the discovery and timing observations, and we describe our data analysis, timing procedure and results in Section 3. Individual sources of interest are discussed in Section 4. Section 5 presents a search for gamma-ray pulsations in Fermi data associated with our pulsars. We compare the properties of pulsars found by PALFA to those of the observed population of radio pulsars in the Galactic plane in Section 6. Given the (early) termination of the PALFA survey in 2020 August, we provide an update on the survey status and sky coverage in Section 7. Finally, we summarize our results in Section 8.

2. Observations

2.1. Survey Observations and Discoveries

Survey data were collected with the ALFA receivers, which consisted of seven beams with half-power widths of 3.6°, and data were recorded with the Mock spectrometers²⁵. This backend-processed two overlapping 172 MHz bands which, once combined and the two polarizations summed, provided 323 MHz of bandwidth centered at 1375.5 MHz and 960 frequency channels sampled every 64 μs. PALFA targeted two regions of the Galactic plane ($|b| < 5^\circ$): the “inner” Galaxy ($32^\circ \lesssim l \lesssim 77^\circ$) and the “outer” Galaxy ($168^\circ \lesssim l \lesssim 214^\circ$). Integration times were 268 s and 180 s for inner and outer Galaxy observations, respectively. Additional details on survey observations for PALFA, including the strategy for surveying the inner and outer Galaxy regions, are provided in Section 7.

Survey data have been processed and searched by three independent pipelines. The first is a reduced-resolution “Quicklook” pipeline performed in near real time on site that enables rapid discovery of bright, nearby pulsars (Stovall 2013). The second is a full-resolution PRESTO²⁶-based pipeline (Ransom 2011). The latter processes data on the Béluغا supercluster, a Compute Canada/Calcul Québec facility hosted at the École de technologie supérieure in Montréal. It searches for dispersed periodic signals in the Fourier domain as well as in the time domain with a fast-folding algorithm (FFA; Parent et al. 2018). Sporadic pulses such as those emitted by RRATs and FRBs are searched for with a single-pulse pipeline (Patel et al. 2018). Lastly, data are searched for pulsars, particularly those in compact orbits, using the Einstein@Home²⁷ pipeline (E@H) described in Allen et al. (2013).

Approximately 40% of the 72 objects we study in this work were first found by either the Quicklook or E@H pipelines. The remaining sources were only found by the full-resolution pipeline. The pipeline search algorithm that identified each source is listed in Table 1 along with the date of discovery. The pulsars’ time-integrated pulse profiles are shown in Figure 1.

2.1.1. Additional Pulsar Discoveries

We also report on the recent discovery of 23 additional pulsars in the PALFA survey. Discovery parameters and estimates of their pulsed flux densities are listed in Table 2, and

²³ www.naic.edu/alfa/pulsar/

²⁴ All PALFA discoveries can be found here: www.naic.edu/~palfa/newpulsars/.

²⁵ www.naic.edu/~astro/mock.shtml

²⁶ <https://github.com/scotransom/presto>

²⁷ <https://einsteinathome.org/>

Table 1
List of Pulsar Discoveries

Previous Name(s)	Ref.	Name	Discovery Date	Pipeline(s)
J1843+01	(4)	J0608+1635	2013 04 18	FFT, SP
		J1843+0119	2017 10 01	SP
		J1849+0106	2013 11 25	FFT, SP
		J1849+0430	2016 10 14	Quicklook
J1852+0000	(3)	J1851+0241	2012 03 27	E@H
		J1852-0000	2015 06 04	FFT, Quicklook
		J1853+0029	2015 09 23	E@H
J1853+03	(2)	J1853+0259	2011 12 15	FFT, SP
J1853+04	(4)	J1853+0427	2015 12 10	SP
J1854+00	(1,2)	J1854+0050	2013 09 15	FFT, SP
		J1855+0306	2012 02 27	E@H
		J1855+0626	2018 06 08	FFT
J1856+0911 / J1856+09	(3,4)	J1856+0912	2016 06 20	FFA, SP
J1858+02	(2)	J1858+0239	2010 01 06	SP
		J1859+0345	2013 07 29	E@H
		J1902+1141	2017 05 25	Quicklook, SP
J1902+02	(2)	J1902+0235	2014 02 24	FFT
J1903+04 / J1903+0415	(1,2)	J1903+0415	2013 09 05	FFT, SP
		J1903+0912	2015 08 26	Quicklook
		J1904+0056	2018 09 19	FFT
J1906+0725	(2)	J1905+1034	2011 10 30	FFT, SP
		J1906+0724	2013 09 10	FFT
		J1907+0833	2011 04 30	Quicklook
J1907+05	(2)	J1908+0558	2014 07 27	FFT
Cand. J1908+13	(4)	J1908+1351	2017 07 27	SP
J1910+1027	(2)	J1909+1205	2011 12 14	E@H
		J1910+0435	2015 09 28	Quicklook
		J1910+0710	2014 10 15	E@H
J1911+09	(2)	J1910+1017	2011 11 04	E@H
		J1910+1026	2011 11 05	FFT
		J1911+0921	2011 11 14	FFT
J1911+10	(2)	J1911+0925	2012 07 23	E@H
		J1911+1051	2014 09 09	FFT
		J1911+1301	2015 12 08	FFT
J1913+1103	(2)	J1911+1336	2017 06 15	FFT
		J1913+0523	2017 10 10	FFT
		J1913+11025 ^a	2011 09 15	FFT
J1915+1144	(2)	J1914+0625	2014 04 07	FFT, SP
		J1914+0805	2017 05 18	FFT
		J1914+0838	2012 10 09	FFT
J1915+1149	(2)	J1914+1428	2012 01 09	E@H
		J1915+0639	2014 01 24	FFT, SP
		J1915+1145	2011 09 15	FFT
J1918+1310	(2)	J1915+1150	2012 09 24	FFT
		J1918+1311	2012 09 12	FFT
		J1921+0921	2016 07 18	Quicklook
J1921+16	(2)	J1921+1630	2014 02 07	FFT
J1924+1628	(2)	J1924+1628	2014 01 14	FFT
J1924+17	(2)	J1924+1713	2011 11 07	FFT
J1926+1613	(2)	J1924+1917	2017 19 19	FFT
		J1926+1614	2014 03 10	FFT
		J1928+1725	2013 11 12	FFT, SP
J1930+14	(2)	J1930+1408	2011 09 15	FFT
		J1930+1722
J1934+19	(2)	J1931+1817	2015 02 21	Quicklook
		J1934+1926	2011 09 15	FFT
		J1935+1829	2015 09 25	FFT
J1936+20	(2)	J1936+2042	2013 09 08	FFT
		J1938+2659	2018 11 17	Quicklook
		J1939+2609	2018 11 17	Quicklook
J1950+3000	(3)	J1948+1808	2018 12 13	Quicklook
		J1948+2819	2015 01 05	E@H
		J1950+3001	2015 05 28	Quicklook, FFA
		J1952+2513	2011 10 27	E@H

Table 1
(Continued)

Previous Name(s)	Ref.	Name	Discovery Date	Pipeline(s)
J1952+3022 / J1952+30	(3,4)	J1952+3021	2015 07 20	FFA, SP
		J1953+2819	2015 01 02	E@H
		J1954+2529	2014 10 24	Quicklook
		J1955+2930	2015 06 22	E@H
J1958+30	(4)	J1958+3033	2015 09 03	SP
J2000+2921 / J2000+29	(3,4)	J2000+2920	2015 11 24	FFA, SP
		J2003+2916	2015 01 25	Quicklook
		J2008+3139	2015 06 19	Quicklook

Note. For each source, we indicate the previous name and respective reference, the definitive name from the timing position obtained in this work, and the pipeline used for the discovery. The discovery dates provided here refer to the date when pulsars were identified in the data. PALFA references are, by order of publication: (1) Zhu et al. (2014), (2:) Lazarus et al. (2015), (3) Parent et al. (2018), (4) Patel et al. (2018); the non-PALFA reference is (5) Lorimer et al. (2013). If no reference is indicated, this work. The pipelines used are as follows: Quicklook (Stovall 2013), Einstein@Home (E@H; Allen et al. 2013) and the main PRESTO-based pipeline (Lazarus et al. 2015), which includes a Fourier-domain periodicity search (FFT), a fast-folding algorithm (FFA; Parent et al. 2018) and a single-pulse search (SP; Deneva et al. 2009; Patel et al. 2018).

^a Extra digit was added to the name to differentiate this pulsar from PSR J1913+1102, a PALFA-discovered double-neutron-star system (Lazarus et al. 2016; Ferdman et al. 2020).

Table 2
Pulsars Recently Discovered by PALFA

PSR (J2000)	P (ms)	DM (pc cm $^{-3}$)	S_{1400} (μ Jy)
J1835+00	790.1	134.3	80(20)
J1837+03	10.70	115.7	57(15)
J1840+03	5.83	80.9	150(40)
J1843+04	397.3	266.1	55(15)
J1847+01 ^a	3.46	20.1	90(20)
J1851+00 ^a	22.84	107.6	67(16)
J1853+00 ^a	33.40	192.2	79(19)
J1857+07	29.12	159.6	52(14)
J1905+04	894.1	384.0	45(12)
J1905+17	278.1	175.4	74(19)
J1916+21	829.2	173.1	51(14)
J1919+04	3.96	142.7	110(30)
J1927+08	253.4	224.0	160(40)
J1935+11	5.39	69.5	90(20)
J1936+13	4.34	168.0	65(17)
J1936+18 ^a	58.35	126.1	38(11)
J1936+21 ^a	31.60	75.0	45(12)
J1936+24	1.90	94.4	120(30)
J1940+14	1274.4	69.9	130(50)
J1940+25	5.89	30.9	70(20)
J1940+26 ^a	4.81	171.6	29(9)
J1944+16	2.43	170.9	170(50)
J1945+17	604.2	167.7	48(13)

Note. Average pulsed flux densities at 1400 MHz, S_{1400} , were estimated using the approach described in Section 3.2.

^a Pulsars redetected by the FAST Galactic Plane Pulsar Snapshot survey (Han et al. 2021) provide higher precision on the position and/or dispersion measure parameters.

their pulse profiles are shown in Figure 2. Supplemental information such as diagnostic plots and the center position of the ALFA beam in which the pulsars were discovered can be found on the survey discovery page. Timing results and/or other notable properties will be reported in future publications (Parent et al., in prep.; Haniewicz et al., in prep.; Doskoch et al., in prep.); the analyses and results presented in the remaining sections of this paper pertain to the aforementioned set of 72 pulsars (Table 1 and Figure 1).

2.2. Timing Observations

Timing observations were largely conducted with Arecibo and, for the 33 strongest sources, with the 76 m Lovell Telescope at Jodrell Bank Observatory (JBO) in Macclesfield, UK. Until 2014, some limited amount of timing data was collected for six of our pulsars with the 100 m Green Bank Telescope (GBT) at the Green Bank Observatory (GBO) in West Virginia, US. In 2020 May, we began follow-up observations on five other sources with the Canadian Hydrogen Intensity Mapping Experiment (CHIME) telescope²⁸ (CHIME/Pulsar Collaboration et al. 2021), located at the Dominion Radio Astrophysical Observatory (DRAO) in British Columbia, Canada. More information on observations for individual sources such as observation sites, cadence, and time span of observations can be inferred from plots introduced in Section 3.1.

At the AO, timing data were collected with the L-wide receiver and recorded with the Puerto Rican Ultimate Pulsar Processing Instrument²⁹ (PUPPI) backend at a central frequency of 1380 MHz with a nominal 800 MHz bandwidth split into 4096 channels sampled every 40.96 μ s. Following radio frequency interference (RFI) excision, the usable bandwidth was typically \sim 600 MHz, and integration lengths ranged from 300 to 1500 s, depending upon the pulsar brightness. Initially, data were recorded in incoherent search mode, but as a pulsar ephemeris improved we switched to fold-mode observations where data were coherently dedispersed at the pulsar dispersion measure (DM) and folded into 10 s subintegrations in real time, modulo the instantaneous pulsar period, producing time-integrated pulse profiles for all frequency channels.

Timing data obtained with the Lovell Telescope were processed using a digital filterbank (DFB), which Nyquist sampled a 512 MHz band at 8-bit resolution and channelised it into 1024 channels using a polyphase filter. After RFI cleaning, the resultant band spanned the range 1350 to 1700 MHz. The data are incoherently dedispersed and folded into 10 s long subintegrations with 1024 pulse phase bins. Observation durations ranged from 30 to 60 minutes depending on the

²⁸ <https://chime-experiment.ca/en>

²⁹ <https://www.naic.edu/puppi-observing/>

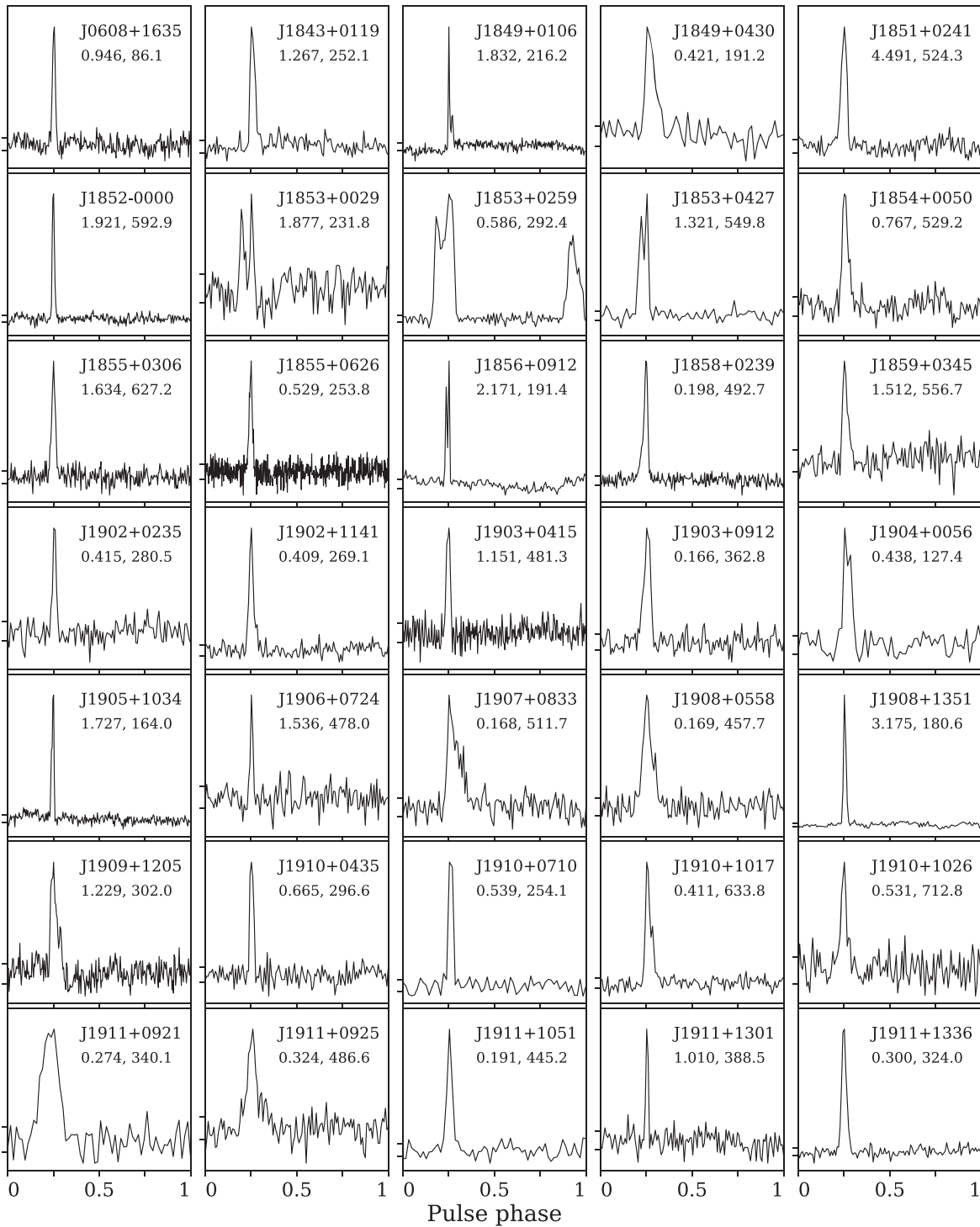


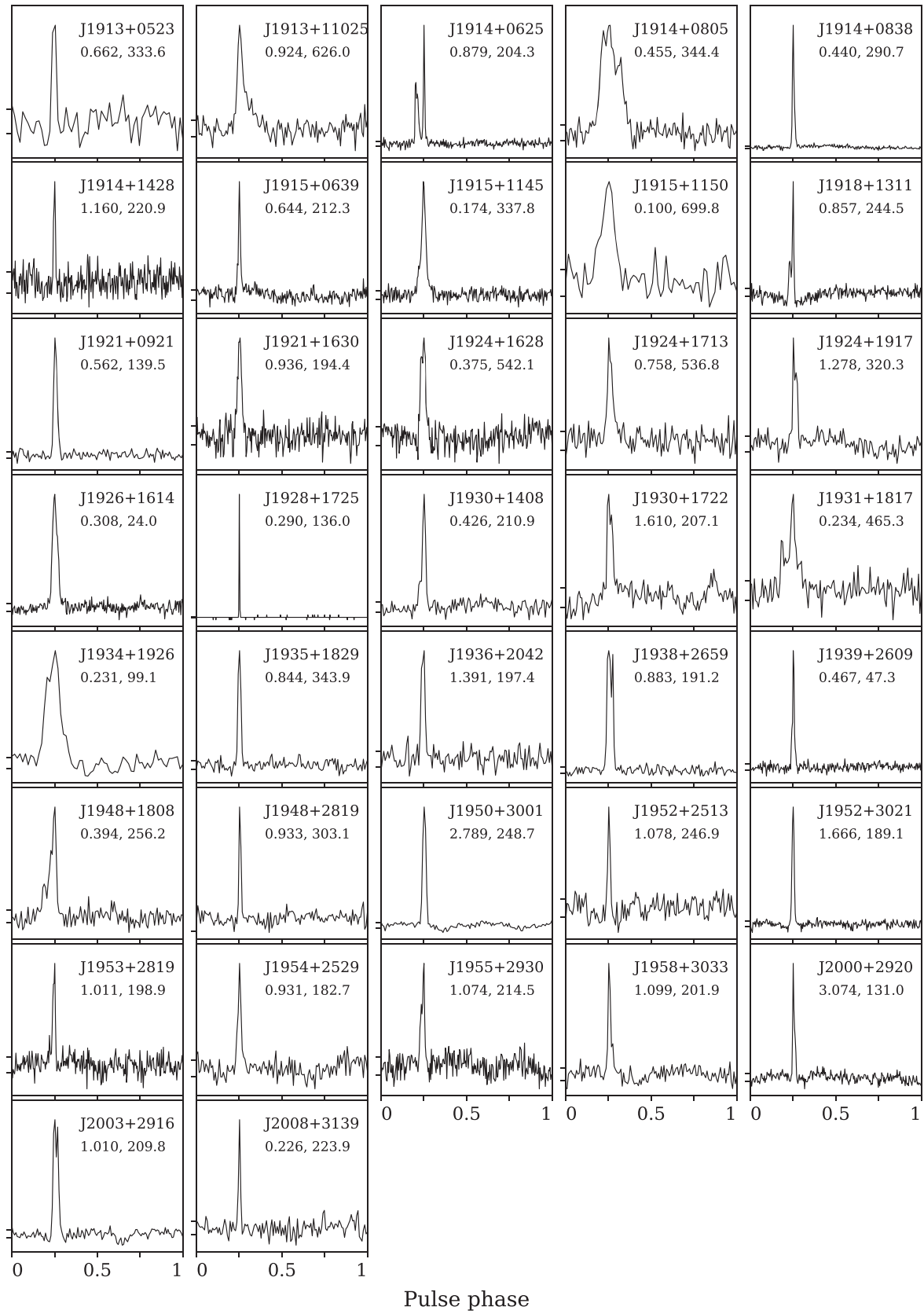
Figure 1. Integrated pulse profiles, generated from Arecibo data at 1.4 GHz, from which template profiles were generated. The name, spin period (s) and dispersion measure (pc cm^{-3}) of each pulsar are listed above their corresponding profile. Depending on the pulsar brightness, the pulse phase resolution varies between 64 and 512 bins. Tick marks on the vertical axis of each panel represent the rms intensity level of the off-source region. We note that only the single-peaked emission mode of PSR J1858+0239 and the normal mode of PSR J1914+0625 are plotted here. Other variants of their average profiles are shown in Sections 4.1.2 and 4.1.3, respectively.

source flux density. More information can be found in Lyne et al. (2017b).

Observations with GBT were recorded with the Green Bank Ultimate Pulsar Processing Instrument (GUPPI; DuPlain et al. 2008) backend, which processes 800 MHz of bandwidth centered at 1.5 GHz. Coherent-dedispersion mode data were

recorded into 512 frequency channels and folded into subintegrations every 10 s.

As for CHIME observations, the stationary instrument operates in the 400–800 MHz frequency range and beam-formed data were collected with the CHIME/Pulsar backend. The latter discretizes the observing band into 1024 baseband

**Figure 1.** (Continued.)

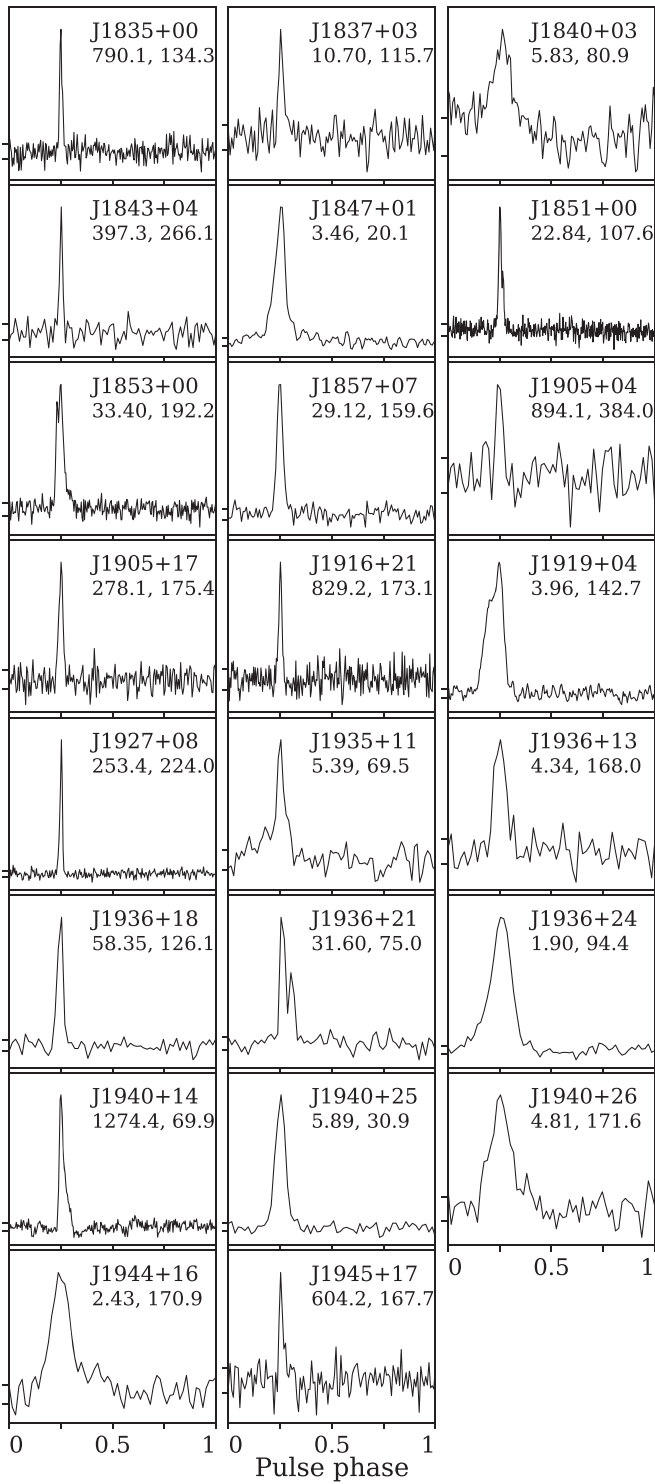


Figure 2. Integrated pulse profiles of 23 additional pulsars recently discovered in the PALFA survey, generated from Arecibo data at 1.4 GHz. Similar to Figure 1, the name, spin period (ms) and dispersion measure (pc cm^{-3}) of each pulsar are listed above their corresponding profile and tick marks on the vertical axis represent the rms intensity level of the off-source region.

channels which are then coherently dedispersed. The Digital Signal Processing for Pulsars (DSPSR) suite³⁰ is used to fold the data into 10 or 30 s subintegrations, depending on the source's DM. The duration of any given observation at CHIME

is limited by the transit time as set by the decl., δ , of each pulsar. On average, the five objects we followed up with CHIME (all with $16^\circ \lesssim \delta \lesssim 27^\circ$) were observed for ~ 15 minutes each per day. More information on the CHIME/Pulsar system can be found in CHIME/Pulsar Collaboration et al. (2021).

3. Data Analysis

3.1. Timing Analysis

In order to calculate the times of arrival (TOAs) of radio pulses in our data sets, we first excised RFI. Where only AO search-mode data were available, the cleaned raw data were folded at the topocentric period and DM that yielded the strongest detection with PRESTO's `prepfold` tool. We then produced a standard profile template by fitting one or more Gaussian components to the integrated profile that was detected with the highest signal-to-noise ratio (S/N). TOAs were then extracted by cross-correlating the folded data with the standard template using the `get_TOAs.py` program from PRESTO, which fits for a linear phase gradient in the Fourier domain to determine the shifts between the profiles and the standard template (Taylor 1992).

When analyzing fold-mode data, we constructed improved, high-S/N standard templates by summing in phase the pulse profiles from multiple observations with the `psradd` tool from the PSRCHIVE³¹ software package. As profiles were being combined, weights were applied based on the S/N of the pulsar signal in each data set. We then set profile baselines to zero to create noise-free templates before smoothing the final profiles with PSRCHIVE's `psrsmooth` tool. TOAs were then extracted using the Fourier phase gradient approach with `pat`, also from the PSRCHIVE package. Given the difference in observing frequencies and the time delays introduced by backend systems, a separate standard profile template was generated to analyze data collected at each site.

The timing analysis was carried out with the TEMPO software package³², which implements a χ^2 minimization technique to compute the best-fit parameters of a timing model. The JPL DE436 planetary ephemeris³³ and the UTC(NIST) time standard³⁴ were used. The basic timing model for each source was parameterized by the pulsar period and first period derivative, P and \dot{P} , R.A., decl., and DM. To fit for DM, we extracted TOAs at different frequencies for a number of epochs using between two and eight frequency subbands per epoch, depending on the signal strength. Arbitrary time offsets between TOAs collected at different observatories were also allowed (where applicable) as timing parameters. Orbital parameters were also included in the timing model of the binary pulsar PSR J1954+2529, which we describe later in Section 4.7. In some cases, we additionally fit for higher-order frequency derivatives to reduce scatter due to the timing noise, an effect that arises from spin irregularities that are intrinsic to the pulsar (Manchester & Taylor 1977). For the five pulsars that displayed glitch activity (Section 4.5), glitch parameters were also computed with TEMPO.

Best-fit timing parameters are provided in Table 3, and corresponding postfit residuals, with rms values that range from

³¹ <http://psrchive.sourceforge.net/>

³² <http://tempo.sourceforge.net/>

³³ <https://naif.jpl.nasa.gov/pub/naif/JUNO/kernels/spk/de436s.bsp.lbl>

³⁴ <https://www.nist.gov/>

Table 3
Best-fit Parameters of the Timing Models

PSR (J2000)	R.A. (J2000) (h:m:s)	Decl. (J2000) (d:m:s)	P (s)	\dot{P} (10^{-15})	DM (pc cm $^{-3}$)	Epoch (MJD)	Data Span (yr)	σ_{res} (ms)
J0608+1635	06:08:51.662(5)	+16:35:09.4(4)	0.945844752002(3)	13.51042(18)	86.08(3)	57584.00	9.3	0.63
J1843+0119	18:43:23.90(3)	+01:19:27.1(8)	1.26699835538(3)	3.758(7)	252.1(^c)	58575.00	1.9	1.85
J1849+0106	18:49:55.404(7)	+01:06:22.6(2)	1.83225931855(9)	17.0080(9)	216.24(15)	57016.00	3.0	0.42
J1849+0430	18:49:40.44(2)	+04:30:36.8(6)	0.42112580396(9)	0.1137(11)	191(1) ^c	58073.00	2.3	1.99
J1851+0241	18:51:20.34(3)	+02:41:20.0(9)	4.4913183586(5)	22.568(14)	524.3(7)	56240.00	2.2	2.52
J1852-0000	18:52:40.167(9)	-00:00:25.5(3)	1.92066632921(2)	251.9666(3)	593(1) ^c	58205.00	5.7	1.29
J1853+0029	18:53:17.745(17)	+00:29:23.8(7)	1.8767576226(3)	2.431(2)	232(4) ^c	57826.00	3.5	2.38
J1853+0259	18:53:14.979(8)	+02:59:47.9(3)	0.585552887667(3)	0.11225(9)	292.4(4)	57093.00	6.8	0.97
J1853+0427	18:53:47.007(13)	+04:27:41.2(5)	1.32065850582(15)	2.645(1)	550(2) ^c	57890.00	3.3	1.06
J1854+0050	18:54:43.47(2)	+00:50:17.8(6)	0.76727953408(2)	0.5775(18)	529.2(7)	56854.00	1.9	1.08
J1855+0306	18:55:38.30(2)	+03:06:22.7(7)	1.6335656928(3)	7.0029(4)	627(2)	57548.00	8.6	2.74
J1855+0626 ^a	18:55:25	+06:26:53	0.5288321(9)		253.8(2)	58375.00	0.7	
J1856+0912	18:56:33.40(1)	+09:12:29.7(3)	2.1707012972(15)	2.6283(15)	191.4(4)	58135.00	3.3	1.44
J1858+0239 ^b	18:58:18	+02:39:52	0.197644188243(13)	14(1)	492.71(2)	56441.00	1.1	
J1859+0345	18:59:12.71(2)	+03:45:57(1)	1.51150850359(2)	0.6478(9)	557(6) ^c	57354.00	6.1	5.42
J1902+0235	19:02:31.062(4)	+02:35:14.75(11)	0.415394227732(2)	0.0948(2)	280.49(14)	56835.00	2.0	0.34
J1902+1141	19:02:02.201(5)	+11:41:05.50(9)	0.40914018296(6)	2.59192(13)	269.12(17)	58377.00	2.5	0.42
J1903+0415	19:03:28.321(17)	+04:15:07.6(6)	1.15139859175(13)	0.2268(5)	481(3) ^c	57450.00	5.4	2.77
J1903+0912	19:03:42.101(5)	+09:12:41.69(16)	0.166314477824(3)	14.8383(2)	362.8(1)	57605.00	2.0	0.33
J1904+0056	19:04:07.06(3)	+00:56:59(1)	0.43808945697(2)	0.004(3)	127(2)	58677.00	1.7	3.81
J1905+1034	19:05:20.625(14)	+10:34:27.7(4)	1.72681020359(3)	20.6980(8)	164.0(6) ^c	57737.00	8.2	1.17
J1906+0724	19:06:22.577(18)	+07:24:22.8(6)	1.5364901376(2)	2.9990(6)	478(4) ^c	57080.00	7.7	3.09
J1907+0833	19:07:57.044(3)	+08:33:59.99(7)	0.167627579462(16)	3.69542(6)	511.68(16)	56161.00	2.6	0.29
J1908+0558	19:08:01.997(6)	+05:58:33.94(18)	0.168677558616(3)	2.2796(3)	457.7(2)	57632.00	4.5	0.65
J1908+1351	19:08:35.31(4)	+13:51:40(1)	3.174831829(8)	3.7(2)	180.59(19)	58489.00	3.0	0.55
J1909+1205	19:09:51.47(5)	+12:05:47(2)	1.229312421(2)	3.40(5)	302(1) ^c	55897.00	3.2	1.39
J1910+0435	19:10:11.072(6)	+04:35:29.5(2)	0.664679416494(9)	17.2366(3)	297(1)	57862.00	3.2	0.87
J1910+0710	19:10:13.873(15)	+07:10:46.4(5)	0.53864678794(3)	0.205(2)	254.1(4)	57671.00	5.5	0.64
J1910+1017	19:10:26.124(2)	+10:17:54.09(6)	0.411158865683(4)	5.41520(7)	633.83(16)	55938.00	3.6	0.22
J1910+1026	19:10:48.753(9)	+10:26:52.5(5)	0.53149303397(2)	257.067(4)	712.8(5)	56334.00	1.4	1.03
J1911+0921	19:11:46.487(9)	+09:21:56.8(3)	0.273706758194(2)	0.01751(18)	340.1(6)	56041.00	3.3	1.19
J1911+0925	19:11:59.472(12)	+09:25:32.2(6)	0.323857547341(5)	3.5480(7)	486.6(5)	55982.00	3.0	1.03
J1911+1051	19:11:42.262(8)	+10:51:26.74(16)	0.190872844929(12)	12.16555(16)	445.21(17)	56578.00	6.1	0.40
J1911+1301	19:11:31.739(9)	+13:01:26.6(3)	1.01046173336(9)	1.8899(6)	389(2)	57915.00	3.5	1.52
J1911+1336	19:11:59.541(3)	+13:36:55.00(7)	0.299992040976(1)	0.15860(7)	323.95(14)	58410.00	3.0	0.43
J1913+0523	19:13:22.721(7)	+05:23:58.8(3)	0.661997424287(7)	1.7969(3)	333.6(3)	58290.00	3.8	1.31
J1913+11025	19:13:42.715(8)	+11:02:58.8(2)	0.923871917718(11)	0.3404(17)	626.0(4)	56356.00	1.6	1.13
J1914+0625	19:14:08.359(3)	+06:25:00.97(5)	0.878889431192(9)	0.4531(11)	204.33(5)	56964.00	3.1	0.15
J1914+0805	19:14:05.508(9)	+08:05:12.7(2)	0.455499390131(6)	0.0302(7)	344.4(2)	58528.00	1.6	1.03
J1914+0838	19:14:26.4506(14)	+08:38:45.14(3)	0.440039882669(4)	0.586395(4)	290.70(11)	56825.00	9.2	0.14
J1914+1428	19:14:53.946(8)	+14:28:46.2(2)	1.15951978505(6)	2.1814(6)	220.9(4)	56000.00	3.4	0.90
J1915+0639	19:15:54.327(2)	+06:39:46.21(4)	0.64414015325(3)	1.8435(4)	212.32(5)	57374.00	5.4	0.13
J1915+1145	19:15:33.1231(8)	+11:45:40.98(2)	0.173647195715(2)	0.01531(3)	337.78(3)	56367.00	1.6	0.09
J1915+1150	19:15:16.61(6)	+11:50:35.4(9)	0.10004095461(3)	13.671(1)	699.83(12)	55927.00	3.2	0.28
J1918+1311	19:18:46.220(5)	+13:11:24.51(13)	0.856748867762(6)	2.2579(6)	244.5(3)	56866.00	1.9	0.61
J1921+0921	19:21:53.487(9)	+09:21:30.2(2)	0.562302288458(14)	9.576(1)	139.5(2)	58119.00	3.1	0.39
J1921+1630	19:21:00.142(18)	+16:30:55.8(9)	0.93644800775(19)	22.345(2)	194.4(5)	56891.00	1.7	1.36
J1924+1628	19:24:44.090(6)	+16:28:37.69(16)	0.375082251011(14)	0.32096(6)	542(1) ^c	57514.00	5.1	1.19
J1924+1713	19:24:32.517(19)	+17:13:33.0(3)	0.758433236391(9)	0.1130(17)	536.8(6)	56055.00	3.2	1.19
J1924+1917	19:24:26.21(4)	+19:17:24.4(3)	1.27794162459(4)	0.199(8)	320.3(6)	58528.00	1.6	1.72
J1926+1614	19:26:50.202(3)	+16:14:18.77(9)	0.308305907254(15)	0.03353(4)	24.02(18)	57589.00	4.7	0.40
J1928+1725 ^a	19:28:52	+17:25:29	0.28983833(8)		135.96(12)	57696.00	5.3	
J1930+1408	19:30:18.9526(18)	+14:08:55.39(5)	0.425720327378(5)	0.00190(1)	210.87(13)	56885.00	8.6	0.21
J1930+1722	19:30:30.11(2)	+17:22:53.2(6)	1.60970633781(2)	0.8808(7)	207(7) ^c	57656.00	6.2	4.10
J1931+1817	19:31:52.739(4)	+18:17:00.77(8)	0.234131440128(17)	107.3637(5)	465(1)	58156.00	6.0	0.72
J1934+1926	19:34:21.651(6)	+19:26:35.31(14)	0.230984425819(16)	0.00268(8)	99.1(3)	55977.00	3.6	0.80
J1935+1829	19:35:42.91(1)	+18:29:28.1(3)	0.843547910278(9)	2.3207(4)	343.9(6)	57852.00	3.8	1.28
J1936+2042	19:36:27.42(2)	+20:42:04.5(4)	1.39072342303(15)	49.3744(14)	197.4(5) ^c	56065.00	5.8	1.26
J1938+2659	19:38:39.175(6)	+26:59:14.96(14)	0.883331781241(9)	3.2275(5)	191.20(5)	58829.00	2.3	0.67
J1939+2609	19:39:42.3413(14)	+26:09:36.39(4)	0.466962555351(7)	0.0052(4)	47.30(6)	58823.00	2.3	0.11
J1948+1808	19:48:22.129(4)	+18:08:30.15(8)	0.394354427486(4)	0.2271(2)	256.16(7)	58861.00	2.3	0.51
J1948+2819	19:48:38.39(1)	+28:19:20.06(19)	0.932692952758(16)	61.26032(13)	303(2)	58102.00	6.3	1.70
J1950+3001	19:50:53.68(2)	+30:01:42.7(3)	2.78891789352(6)	149.013(1)	249(2)	58162.00	5.5	1.85

Table 3
(Continued)

PSR (J2000)	R.A. (J2000) (h:m:s)	Decl. (J2000) (d:m:s)	P (s)	\dot{P} (10^{-15})	DM (pc cm $^{-3}$)	Epoch (MJD)	Data Span (yr)	σ_{res} (ms)
J1952+2513	19:52:20.738(15)	+25:13:44.1(7)	1.07764729476(8)	1.0648(17)	246.9(5)	55731.00	4.3	1.19
J1952+3021	19:52:19.696(11)	+30:21:20.0(4)	1.66566523108(16)	10.8257(9)	189.1(4)	57821.00	3.6	1.08
J1953+2819	19:53:35.238(11)	+28:19:39.52(19)	1.01100245325(5)	2.14126(17)	199(2)	58094.00	6.2	1.76
J1954+2529	19:54:19.716(3)	+25:29:27.34(7)	0.931210094606(4)	1.25870(7)	182.70(16)	58104.00	6.5	0.73
J1955+2930	19:55:07.527(9)	+29:30:49.80(16)	1.07387774187(7)	3.3574(4)	214(1)	57822.00	3.7	1.29
J1958+3033	19:58:06.82(1)	+30:33:52.7(2)	1.09858060946(1)	6.4576(6)	201.9(4)	57683.00	2.7	0.95
J2000+2920	20:00:16.508(6)	+29:20:07.47(12)	3.07378325868(3)	37.4364(4)	131(1) ^e	58196.00	5.7	1.00
J2003+2916	20:03:03.194(6)	+29:16:00.96(11)	1.0098766696(5)	0.3410(2)	210(1)	57767.00	4.0	0.92
J2008+3139	20:08:39.9874(13)	+31:39:27.36(2)	0.226118635651(2)	0.082764(11)	223.9(2)	57831.00	3.6	0.18

Notes. Numbers in parentheses are the 1σ uncertainties on the last digit reported by TEMPO, after weighting the TOAs such that $\chi^2 = 1$. Best-fit glitch and orbital (PSR J1954+2529) parameters are provided separately in Sections 4.5 and 4.7, respectively. TEMPO-readable ephemeris files containing the solutions listed here are provided on Zenodo: doi:[10.5281/zenodo.5646566](https://doi.org/10.5281/zenodo.5646566).

^a Unsolved timing model.

^b Partially solved timing model.

^c Improved precision from redetection in the FAST Galactic Plane Pulsar Snapshot survey can be found in Han et al. (2021).

86 μ s to 5.4 ms, are shown in Figure 3. Other measured and inferred pulsar properties are listed in Table 4.

Coherent solutions were obtained for all but three pulsars: PSRs J1855+0626, J1858+0239, and J1928+1725. The first pulsar, PSR J1855+0626, is an intermittent pulsar with too few detections to enable phase connection. We discuss its intermittency and emission properties in Section 4.3.1. PSR J1858+0239 is a pulsar whose unstable average profiles appeared to show evidence of mode-changing behavior, which we discuss in Section 4.1. For that source, timing observations were conducted solely with Arecibo and we monitored the pulsar for ~ 1.5 yr. We were able to phase connect a subset of TOAs from ~ 10 consecutive epochs within a dense-observing timing campaign (spanning approximately one month) during which time the average pulse profile remained fairly stable and could thus be analyzed with one common standard profile. Within that TOA set, we detected a significant spin-down rate (see \dot{P} , reported in Table 3). However, when we attempted to connect time gaps between other consecutive pairs of closely spaced observations in which the pulsar displayed similar average profiles, we could not produce a consistent solution. Although we clearly observed a change in the observed spin frequency, an accurate \dot{P} measurement requires that the timing coherence extends over at least one year in order to break the covariance between spin and astrometric parameters. Furthermore, we suspect that magnetospheric activity may coexist with torque variability (Kramer et al. 2006), thus the putative \dot{P} reported in Table 3 may not be representative of the pulsar's normal spin down (see Section 4.1.2). Dedicated, long-integration and regular observations would be required to obtain an accurate description of this pulsar's rotation. Finally, the last unsolved source, PSR J1928+1725, is a RRAT that could only be timed through its single pulses. All timing observations were conducted with Arecibo. A number of bright, narrow single pulses were detected but at a very irregular rate, with clusters of pulses being emitted within a few 15 minute integrations and no detectable emission in several data sets, leaving large time gaps between detections. We extracted topocentric TOAs from each single pulse and attempted to achieve phase connection but were unsuccessful. Similar to PSR J1858+0239, we suspect that PSR J1928+1725

experiences large torque variability. We discuss in more detail the properties of this RRAT in Section 4.4 and the evidence for the possible changes in spin-down rate.

3.2. Flux Density Calculations

We estimated the average pulsed flux densities at 1400 MHz, S_{1400} , by calibrating the ALFA discovery data using the radiometer equation (Dewey et al. 1985). The ALFA receiver provides a nominal bandwidth of 323 MHz, however effective bandwidths typically range between 260 MHz and 300 MHz following RFI excision. The latter, narrower bandwidths were used in the calibration procedure. Sky temperatures at the pulsar positions were estimated by extrapolating the 408 MHz all-sky map from Remazeilles et al. (2015) to 1400 MHz, assuming a spectral index³⁵ of -2.7 (Remazeilles et al. 2015). The system temperatures of the ALFA receiver typically varied between 28 K and 32 K. In estimating the flux density, we assumed a system temperature of 30 K. We used a value of 9 K Jy $^{-1}$ for the gain of the central ALFA beam, and scaled the gain of the outer six beams to be 79% that of the central beam (Cordes et al. 2006). The data-analysis procedure discards any rotation-independent radio flux from the pulsar.

Our average pulsed flux density measurements are reported in Table 4. Considerable systematic uncertainties affect our measurements, arising notably from fluctuations in the system temperature, reductions in the effective gain due to variations in the receiver response and positional offsets between the true position of the pulsars (i.e., timing positions) and the beam center positions. These uncertainties are included in the error estimates reported in Table 4. The same approach was used to estimate the pulsed flux density of the 23 additional pulsar discoveries reported in Table 2 of Section 2.1.1.

We note here that the pulse profiles shown in Figure 1, most of which were created from data collected with the 800 MHz L-Wide receiver at Arecibo, are not the profiles that were used to estimate the average pulsed flux densities. Due to the difference in the spectral response of the ALFA and L-Wide

³⁵ Defined as $S_\nu \propto \nu^\alpha$, where S_ν is the flux density at frequency ν and α is the spectral index.

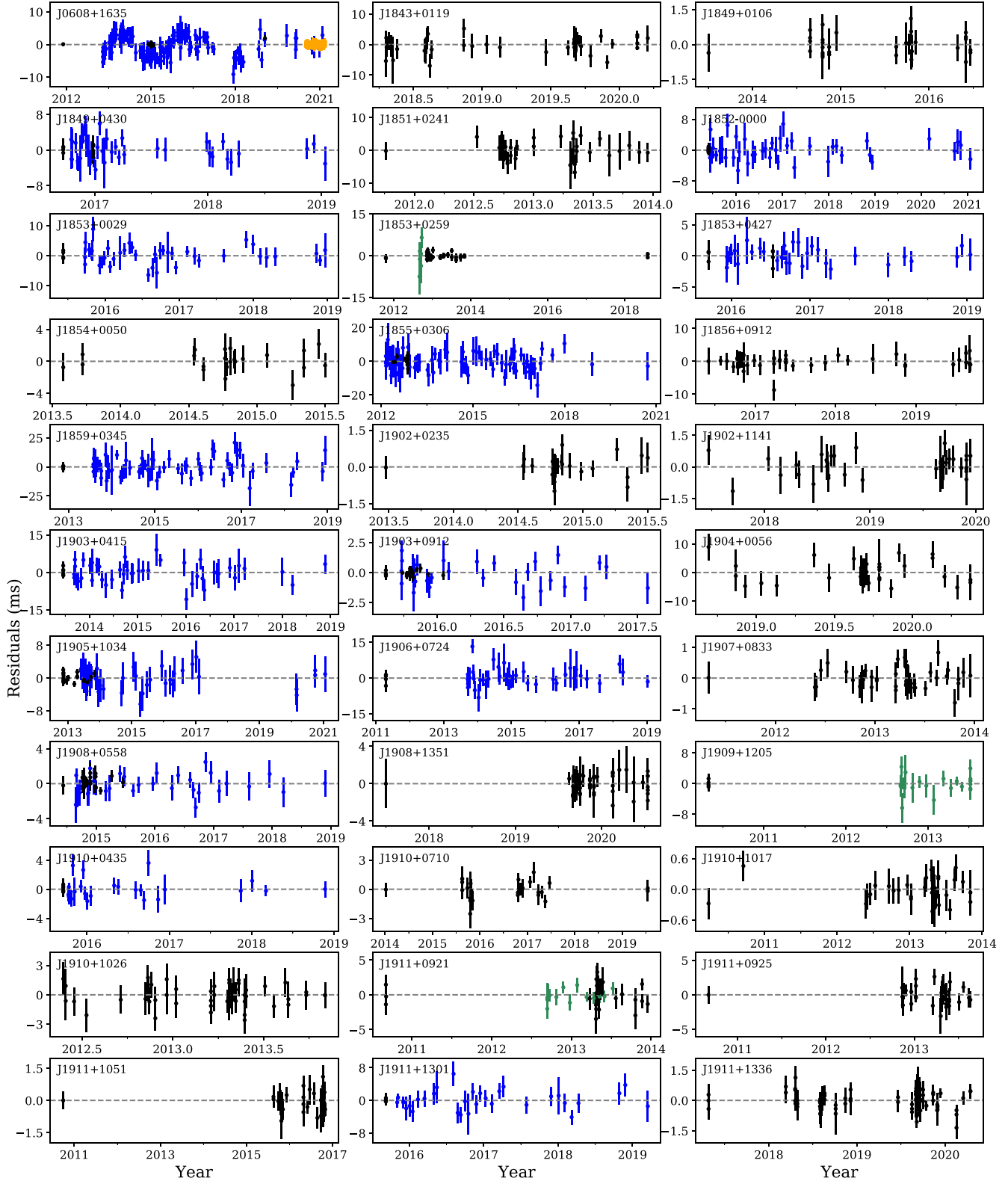


Figure 3. Postfit timing residuals of pulsars with phase-connected timing solutions. TOAs collected at the AO are shown in black, at the JBO in blue, at the GBO in green and with CHIME/Pulsar in orange. We note that the features in the JBO timing residuals of PSR J0608+1635 are likely due to the combined effect of timing noise and the use of a slightly inaccurate initial ephemeris when observing the pulsar in fold mode at the JBO. The features are inconsistent with an orbital motion.

receivers and because pulsars generally have power-law spectra and their pulse profiles evolve with observing frequency, the profiles in Figure 1 cannot be directly normalized to the flux densities reported in Table 4.

3.3. Interstellar Scattering

Integrated pulse profiles were examined to identify asymmetric broadening that would be indicative of frequency-dependent scattering by the turbulent ISM. We attempted to

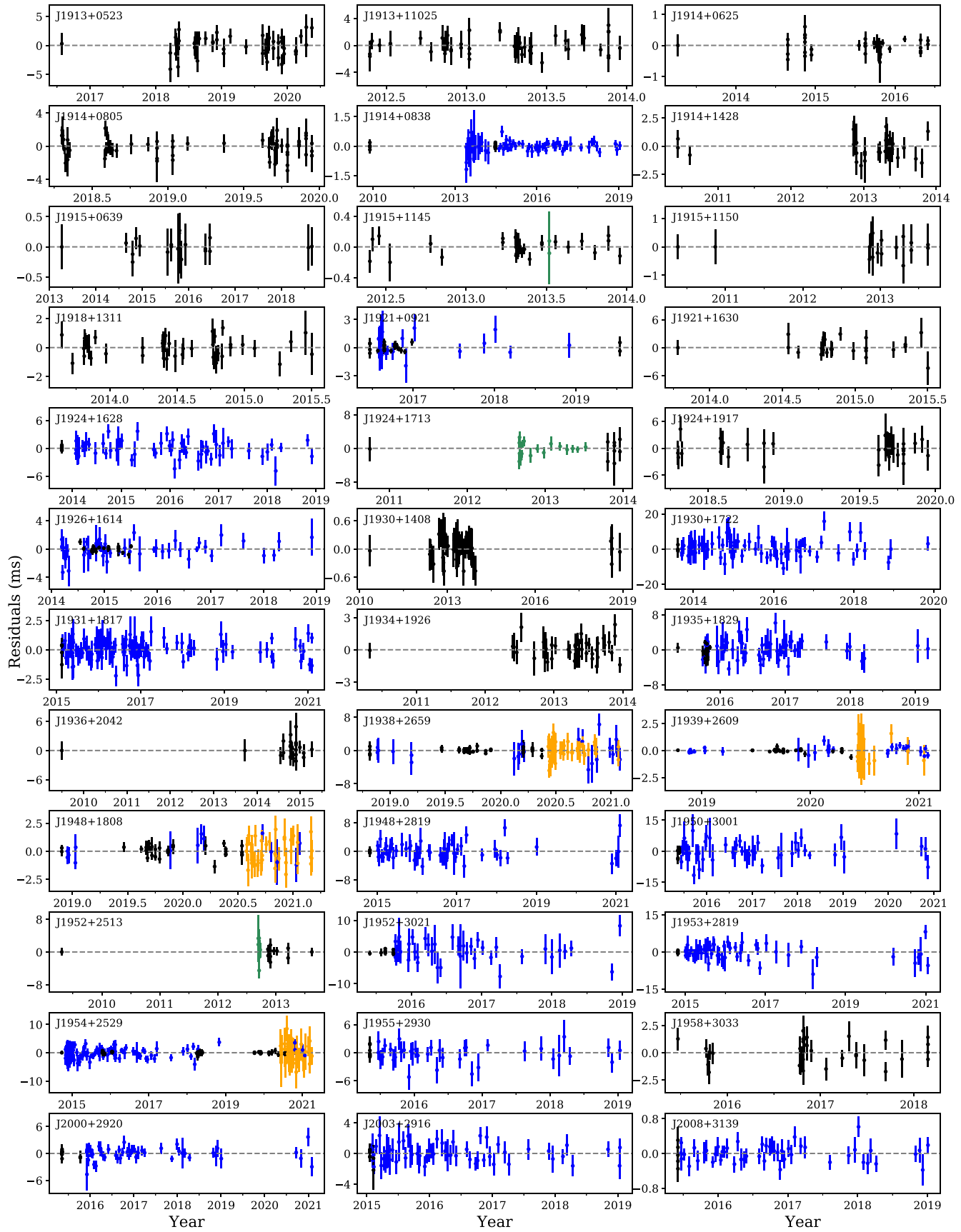


Figure 3. (Continued.)

Table 4
Measured and Derived Pulsar Properties

PSR (J2000)	ℓ ($^{\circ}$)	b ($^{\circ}$)	D_{NE2001} (kpc)	D_{YMW16} (kpc)	W50 (ms)	S_{1400} (μJy)	$\log(\tau_c)$ (yr)	$\log(B)$ (G)	$\log(\dot{E})$ (erg s $^{-1}$)
J0608+1635	193.366	-1.569	2.4	1.7	17(4)	140(40)	6.0	12.6	32.8
J1843+0119	33.195	2.392	6.1	6.1	4(1)	63(16)	6.7	12.3	31.9
J1849+0106	33.744	0.841	5.5	4.6	13(7)	22(6)	6.2	12.8	32.0
J1849+0430	36.748	2.446	5.1	6.0	26(7)	110(30)	7.8	11.3	31.8
J1851+0241	35.314	1.248	9.7	11.3	6(4)	56(14)	6.5	13.0	31.0
J1852-0000	33.066	-0.277	8.2	5.8	27(8)	115(19)	5.1	13.3	33.1
J1853+0029	33.580	-0.19	5.5	4.1	75(15)	74(19)	7.1	12.3	31.2
J1853+0259	35.806	0.963	6.3	5.8	51(5)	220(40)	7.9	11.4	31.3
J1853+0427	37.170	1.512	10.7	15.7	7(2)	100(30)	6.9	12.3	31.7
J1854+0050	34.053	-0.349	7.9	5.7	21(6)	48(8)	7.3	11.8	31.7
J1855+0306	36.175	0.483	9.5	7.4	39(6)	35(6)	6.6	12.5	31.8
J1855+0626 ^a	39.125	2.055	6.5	9.3	10(1)	130(30)			
J1856+0912	41.715	3.058	5.9	9.6	53(17)	40(11)	7.1	12.4	31.0
J1858+0239 ^b	36.085	-0.31	7.9	5.9	11(2)	140(40)	5.3	12.2	34.9
J1859+0345	37.169	-0.01	8.6	6.2	31(12)	90(20)	7.6	12.0	30.9
J1902+0235	36.498	-1.282	8.2	13.9	9(3)	40(11)	7.8	11.3	31.7
J1902+1141	44.537	2.984	5.9	6.1	12(3)	120(30)	6.4	12.0	33.2
J1903+0415	38.088	-0.732	8.1	7.6	30(5)	72(12)	7.9	11.7	30.8
J1903+0912	42.522	1.49	8.5	11.8	6(3)	90(20)	5.2	12.2	35.1
J1904+0056	35.224	-2.387	2.8	4.3	21(7)	45(12)	9.2	10.6	30.3
J1905+1034	43.919	1.755	5.0	6.9	26(7)	40(11)	6.1	12.8	32.2
J1906+0724	41.222	0.074	8.4	6.9	23(12)	45(11)	6.9	12.3	31.5
J1907+0833	42.431	0.262	9.2	8.3	15(1)	100(17)	5.9	11.9	34.5
J1908+0558	40.141	-0.949	8.7	10.6	6(1)	50(13)	6.1	11.8	34.3
J1908+1351	47.206	2.558	6.1	6.9	5(2)	22(6)	7.1	12.5	30.7
J1909+1205	45.780	1.472	7.9	10.1	47(5)	100(30)	6.8	12.3	31.9
J1910+0435	39.158	-2.062	7.3	11.3	15(5)	90(20)	5.8	12.5	33.4
J1910+0710	41.461	-0.879	6.1	6.0	16(8)	32(5)	7.6	11.5	31.7
J1910+1017	44.250	0.517	12.5	13.7	11(6)	37(9)	6.1	12.2	33.5
J1910+1026	44.426	0.503	14.9	15.8	13(4)	58(15)	4.5	13.1	34.8
J1911+0921	43.576	-0.207	5.0	6.4	15(4)	113(18)	8.4	10.8	31.5
J1911+0925	43.654	-0.227	6.9	8.1	19(3)	90(20)	6.2	12.0	33.6
J1911+1051	44.890	0.499	9.0	10.1	7(3)	51(13)	5.4	12.2	34.8
J1911+1301	46.792	1.538	10.5	11.6	16(8)	51(13)	6.9	12.1	31.9
J1911+1336	47.369	1.712	9.2	10.4	8(2)	72(19)	7.5	11.3	32.4
J1913+0523	40.243	-2.395	8.7	16.1	2(1)	25(7)	6.8	12.0	32.4
J1913+11025	45.289	0.151	13.2	11.4	31(7)	140(40)	7.6	11.8	31.2
J1914+0625	41.233	-2.092	5.8	8.3	49(3)	60(16)	7.5	11.8	31.4
J1914+0805	42.708	-1.307	8.1	10.7	29(4)	160(40)	8.4	11.1	31.1
J1914+0838	43.243	-1.124	7.1	8.1	4(2)	280(50)	7.1	11.7	32.4
J1914+1428	48.461	1.487	6.9	6.5	22(9)	57(15)	6.9	12.2	31.7
J1915+0639	41.655	-2.366	6.1	8.9	8(3)	41(11)	6.7	12.0	32.4
J1915+1145	46.129	0.082	8.0	7.2	5.6(7)	90(20)	8.3	10.7	32.1
J1915+1150	46.170	0.18	16.9	14.0	12(2)	47(12)	5.1	12.1	35.7
J1918+1311	47.759	0.055	6.8	6.2	7(3)	54(14)	6.8	12.1	32.2
J1921+0921	44.733	-2.418	4.8	6.1	10(4)	58(15)	6.0	12.4	33.3
J1921+1630	50.949	1.138	6.4	5.1	16(4)	48(13)	5.8	12.7	33.0
J1924+1628	51.337	0.331	14.8	10.5	13(2)	110(30)	7.3	11.5	32.4
J1924+1713	51.975	0.726	15.6	10.9	20(6)	36(6)	8.0	11.5	31.0
J1924+1917	53.782	1.725	9.8	8.6	4(1)	39(11)	8.0	11.7	30.6
J1926+1614	51.367	-0.226	1.9	1.3	8(1)	90(20)	8.2	11.0	31.7
J1928+1725 ^a	52.641	-0.087	4.9	3.7	1.1(6)	1400(400)			
J1930+1408	49.932	-1.962	6.9	5.9	8(3)	51(13)	9.6	10.5	30.0
J1930+1722	52.790	-0.45	6.6	4.7	59(13)	90(30)	7.5	12.1	30.9
J1931+1817	53.739	-0.303	12.9	9.6	18(2)	150(40)	4.5	12.7	35.5
J1934+1926	55.038	-0.256	4.1	3.2	22(4)	130(30)	9.1	10.4	30.9
J1935+1829	54.361	-0.999	9.9	8.6	16(7)	37(11)	6.8	12.2	32.2
J1936+2042	56.376	-0.074	6.6	5.0	40(11)	45(12)	5.6	12.9	32.9
J1938+2659	62.107	2.562	7.2	8.6	26(7)	80(20)	6.6	12.2	32.3
J1939+2609	61.501	1.951	3.1	2.7	4(2)	150(40)	9.2	10.7	30.3
J1948+1808	55.544	-3.782	9.4	11.3	15(3)	80(20)	7.4	11.5	32.2
J1948+2819	64.366	1.307	9.7	11.0	13(7)	46(8)	5.4	12.9	33.5
J1950+3001	66.087	1.749	8.3	8.7	6(2)	240(60)	5.5	13.3	32.4

Table 4
(Continued)

PSR (J2000)	ℓ ($^{\circ}$)	b ($^{\circ}$)	D_{NE2001} (kpc)	D_{YMW16} (kpc)	W50 (ms)	S_{1400} (μJy)	$\log(\tau_c)$ (yr)	$\log(B)$ (G)	$\log(\dot{E})$ (erg s^{-1})
J1952+2513	62.125	-0.98	8.1	8.4	19(8)	31(8)	7.2	12.0	31.5
J1952+3021	66.526	1.65	7.0	7.5	26(13)	23(6)	6.4	12.6	32.0
J1953+2819	64.926	0.374	7.1	7.6	19(4)	47(8)	6.9	12.2	31.9
J1954+2529	62.580	-1.229	6.8	7.8	16(7)	59(16)	7.1	12.0	31.8
J1955+2930	66.116	0.697	7.4	7.6	24(4)	72(19)	6.7	12.3	32.0
J1958+3033	67.350	0.691	7.1	7.3	13(9)	32(9)	6.4	12.4	32.3
J2000+2920	66.549	-0.353	5.4	6.7	26(12)	100(30)	6.1	13.0	31.7
J2003+2916	66.812	-0.903	7.3	7.5	35(8)	200(50)	7.7	11.8	31.1
J2008+3139	69.478	-0.639	7.3	7.2	3(2)	43(11)	7.6	11.1	32.5

Notes. The average pulsed flux density at 1400 MHz, S_{1400} , and the pulse FWHM, W50, were calculated from the ALFA discovery data. The D_{NE2001} and D_{YMW16} parameters are the DM-estimated distances of the pulsars predicted by the NE2001 and YMW16 models, respectively. Numbers in parentheses are 1σ uncertainties on the last digit.

^a Unsolved timing model.

^b Partially solved timing model.

quantify ISM scattering in each source by fitting a temporal pulse-broadening function to the observed pulse profile in different frequency bands. In our model, we assume that the radio waves are scattered isotropically by a single thin scattering screen. The pulse-broadening function associated with this assumption takes the form $\tau_{\text{sc}}^{-1} e^{-1/\tau_{\text{sc}}}$, where τ_{sc} is the characteristic scattering time which scales with observing frequency as $\tau_{\text{sc}}(\nu) \propto \nu^{-\alpha_{\text{sc}}}$.

In the latter expression, α_{sc} is the scattering spectral index. We simultaneously fit the subbanded pulse profiles as a single-component Gaussian convolved with the scattering broadening function, and compared the goodness of the fit to that of a Gaussian mixture that includes up to three components. For several of our low-S/N pulsars, we did not fit subbanded profiles but instead profiles integrated over the entire observing band.

Only four pulsars display pulse shapes that are best described by the scatter broadening model. We show in Figure 4 the fits to the subbanded pulse profiles, and best-fit scattering spectral indices α_{sc} and broadening timescales τ_{sc} at 1 GHz are provided in Table 5 along with the scattering timescales predicted by the NE2001 (Cordes & Lazio 2002) Galactic electron-density model. Another model that has been widely used is the YMW16 (Yao et al. 2017) model, but unlike the NE2001 model, it does not use scattering as a modeling parameter. Instead, it estimates τ_{sc} at 1 GHz for a given DM value based on the empirical scaling between scattering timescale and DM obtained by Krishnakumar et al. (2015). We include those estimates in Table 5, as well. We note significant discrepancies (by up to two orders in magnitude) between the NE2001 predictions and our measurements. These inconsistencies could be attributed to unmodeled foreground structures such as HII regions. New distance and scattering measurements along various lines of sight are thus valuable to construct more complete models of the Galactic electron density in the future.

PSRs J1911+0925 and J1924+1713 have scattering indices consistent with both an isotropic scattering mechanism ($\alpha_{\text{sc}} = 4$; Cronyn 1970) and Kolmogorov turbulence in a cold plasma ($\alpha_{\text{sc}} = 4.4$; Lee & Jokipii 1976; Rickett 1977), but PSRs J1907+0833 ($\alpha_{\text{sc}} = 3.0$) and J1913+11025 ($\alpha_{\text{sc}} = 1.6$) have flatter scattering spectra than the aforementioned theoretical models. Anomalous

scattering arising from structures in the ISM (Cordes & Lazio 2001; Rickett et al. 2009) or anisotropic scattering mechanisms (Stinebring et al. 2001; Tuntsov et al. 2013) could explain the lower α_{sc} values. PSRs J1907+0833 and J1913+11025 also have large DM-estimated distances, both exceeding 8 kpc. As such, their low α_{sc} could also be explained by the presence of multiple scattering screens along their long lines of sight. Dedicated observations would be required to probe the nature of the scattering observed in these pulsars; our flux- and band-limited data sets do not allow us to distinguish between models.

Figure 5 shows the distribution of τ_{sc} at 1 GHz as a function of DM values. For comparison, we additionally plot measurements reported in the ATNF catalog (version 1.65) for other known pulsars. The best-fit solution to the empirical scaling between τ_{sc} and DM from Krishnakumar et al. (2015) at 327 MHz, scaled to a frequency of 1 GHz using the average value of our best-fit α_{sc} measurements, is also shown in Figure 5 (solid line). We see that our sources, which have high DMs and large τ_{sc} , are consistent with the scaling relation from Krishnakumar et al. (2015) for an average α_{sc} of 3.35.

We also note that two low-DM sources, PSRs J1926+1614 (DM = 24.0 pc cm $^{-3}$) and J1939+2609 (DM = 47.3 pc cm $^{-3}$), displayed obvious signs of scintillation features in their spectra. From epoch to epoch, we observed fluctuations in the flux densities of both pulsars ranging from roughly 20 to 200 μJy . Measurement of the scintillation bandwidth, and hence the scattering delay, for these and other low-DM PALFA sources could place complementary constraints to our pulsar broadening measurements for high-DM pulsars. This analysis is, however, beyond the scope of this paper.

4. Pulsar Properties

The pulsars we present in this work are typical in their spin-down properties and representative of the broader population. Figure 6 shows the positions of the 68 pulsars with well-measured \dot{P} on a $P - \dot{P}$ diagram compared to the rest of the known pulsar population. Here, we discuss individual sources having interesting properties, including pulsars that exhibit considerable variability in their radio emission such as mode changing (Section 4.1) and nulling (Section 4.2, and extreme manifestations thereof in Sections 4.3 and 4.4). Our timing

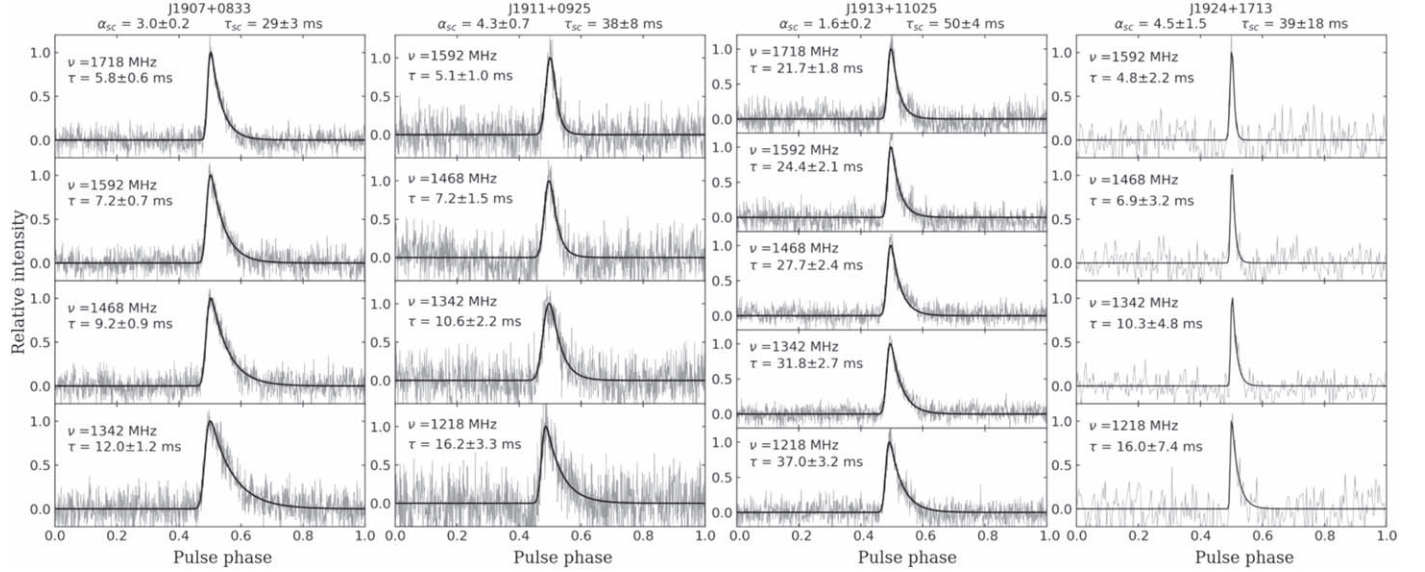


Figure 4. Pulse profiles (gray) in different frequency subbands for the four pulsars that display scatter-broadened profiles, and best-fit pulse-broadening functions (solid black) of the subbanded profiles (see text for model description). Pulsar names, best-fit scattering spectral indices, and characteristic timescales at 1 GHz are listed above each panel (also in Table 5). Within each frequency subpanel, we provide the central observing frequency (ν) of the subband and the scattering time (τ) at that frequency.

Table 5
Best-fit Scattering Parameters for the Four Pulsars with Pulse Profiles Showing Measurable Scatter Broadening

PSR (J2000)	DM (pc cm ⁻³)	α_{sc}	τ_{sc} (ms)	τ_{NE2001} (ms)	$\tau_{\text{knn+15}}$ (ms)
J1907+0833	511.68(16)	3.0(2)	29(3)	5.3	19.0
J1911+0925	486.6(5)	4.3(7)	38(8)	569	15.4
J1913+11025	626.0(4)	1.6(2)	50(4)	4.0	44.3
J1924+1713	536.8(6)	4.5(1.5)	39(18)	0.3	23.3

Note. The scattering timescales, τ_{sc} , listed in the fourth column were scaled to 1 GHz using the pulsar's scattering spectral index, α_{sc} . Scattering timescales at 1 GHz predicted by the NE2001 model (τ_{NE2001}) and the scaling relation obtained by Krishnakumar et al. (2015) ($\tau_{\text{knn+15}}$) are provided in the last two columns.

analysis has also revealed glitch activity in five pulsars (Section 4.5), two of which are young pulsars with characteristic ages ~ 30 kyr (Section 4.6). Another interesting source is PSR J1954+2529, an unusual, nonrecycled pulsar in an eccentric binary system (Section 4.7), which also exhibited a glitch.

4.1. Mode-changing Pulsars

Mode changing (or switching) is a type of discontinuous transition in the radio emission where the average pulse profile abruptly switches between two or more quasi-stable states (Backer 1970a). It is a broadband phenomenon (Bartel et al. 1982) that occurs on variable timescales. Changes in the radio beam emission pattern, and hence in the observed pulse profile, are believed to be the result of a global redistribution in the magnetosphere currents and/or magnetic fields. Mode changing has been recognized in roughly two dozen pulsars thus far (see e.g., Wang et al. 2007; Lyne et al. 2010; Ng et al. 2020). Below we describe the emission of three pulsars that displayed mode-changing behavior.

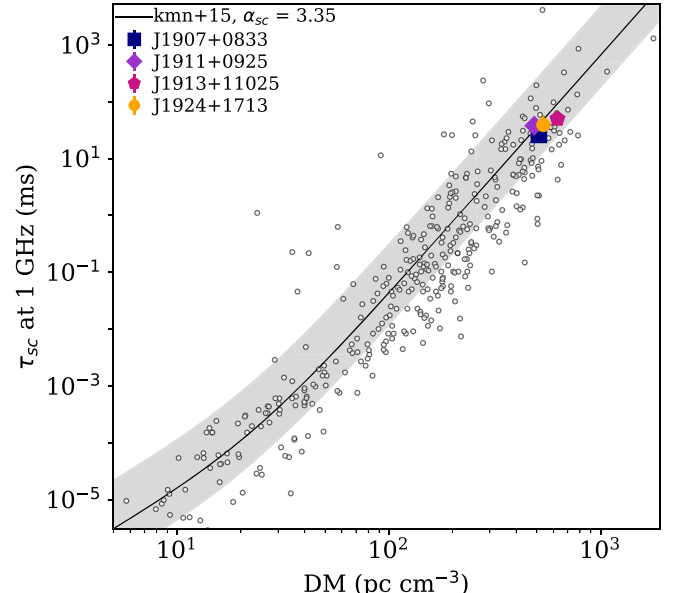


Figure 5. Scattering timescales, τ_{sc} , at 1 GHz vs. DM for objects with reported τ_{sc} measurements in the ATNF catalog (black circles). The four pulsars presented in this work for which we measured scatter broadening are highlighted as color-filled points. The solid line corresponds to the best-fit scaling relation between τ_{sc} and DM obtained by Krishnakumar et al. (2015) at 327 MHz, scaled to 1 GHz using a scattering spectral index of 3.35, which is the average α_{sc} value of our scattered pulsars, while the shaded region is the same relation, also scaled to 1 GHz, but using the range of measured α_{sc} (Table 5).

4.1.1. PSR J1853+0259

PSR J1853+0259 ($P = 585.6$ ms) has a complex pulse profile structure (shown in Figure 7). It exhibits two main components separated by 107° in pulsar rotation phase. The leading component is a weaker, single-peaked pulse of width $W_{50} = 26$ ms (near pulse phase 0.35 in Figure 7), while the main component has a double-peak pulse shape of width

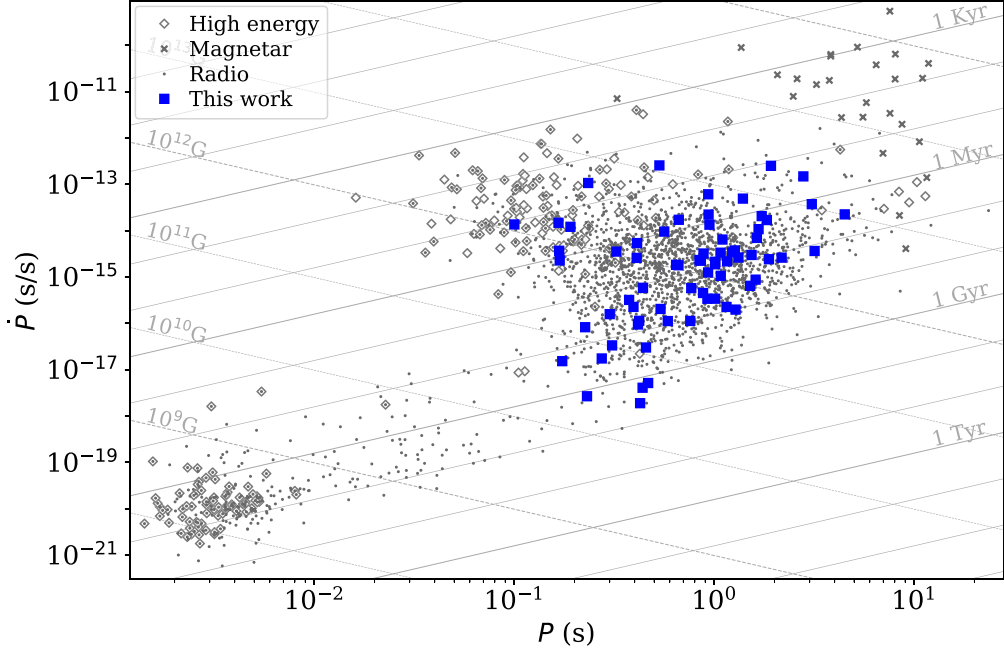


Figure 6. $P - \dot{P}$ diagram showing the periods and period derivatives of known pulsars, separated based on the nature of their emission: gray points are rotation-powered pulsars emitting in radio, diamonds are pulsars emitting at high energies (gamma and/or X-rays), and crosses are magnetars. Pulsars presented in this paper are shown as blue squares. Lines of constant magnetic field (dashed) and characteristic age (solid) are overlaid. P and \dot{P} values for pulsars other than from this work were taken from the ATNF Catalog and the McGill Magnetar Catalog³⁶ (Olausen & Kaspi 2014).

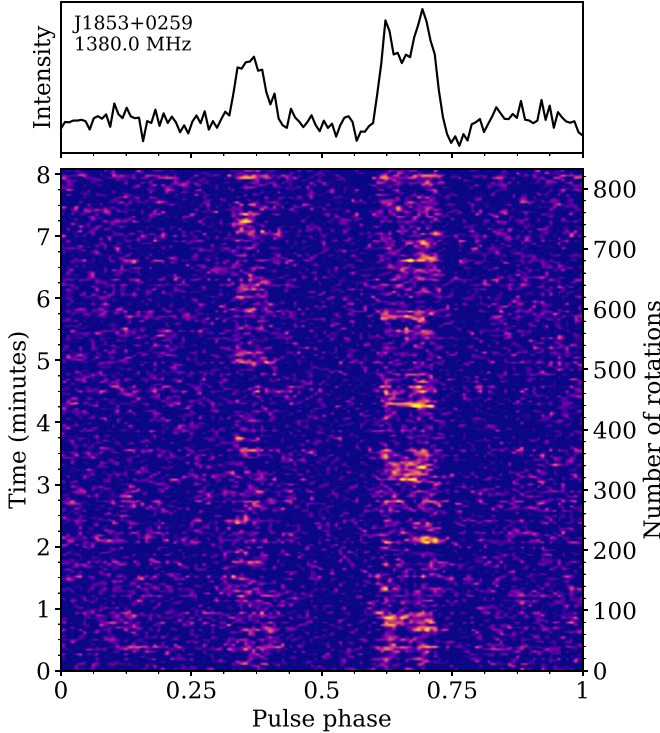


Figure 7. Integrated pulse profile (top panel) and intensity as a function of time and phase (bottom panel), showing temporal intensity variations in the various profile components of PSR J1853+0259. Individual rows in the time vs. phase panel have been averaged over four pulsar rotations. The data shown here were taken with the L-Wide backend at Arecibo on 2018 August 6.

$W_{50} = 62$ ms (near phase 0.65 in Figure 7) and is about two times brighter than the leading component.

The emission of PSR J1853+0259 is notable in that it shows an uncommonly high degree of variability in its profile shape

and intensity from one cycle to the next, to the point where it is comparable to a mode-changing behavior. For approximately 70% of the time, the pulsar is in a transition state where emission is detectable in both components, albeit over a range of phase, shape, and intensity. The second most common state, observed 25% of the time, is the one where the pulsar shows emission only in the main component (phase 0.65). The remaining 5% of the time, emission is present only in the leading pulse. However, the timescales associated with that mode are too short, lasting on average for a dozen rotations of the pulsar, to allow for the average pulse profile to be stable.

4.1.2. PSR J1858+0239

PSR J1858+0239 ($P = 197.6$ ms) exhibits significant jitter noise in its integrated profiles. It appears to switch between two equally prevalent emission modes, displaying either a faint and narrow ($S_{1400} \approx 65 \mu$ Jy, $W_{50} \approx 5$ ms) roughly single-peaked profile or a brighter and wider ($S_{1400} \approx 160 \mu$ Jy, $W_{50} \approx 11$ ms) profile having two peaks. In the latter mode, we have seen large fluctuations in the relative intensity of the leading and trailing peaks from one epoch to the next (see integrated profiles in Figure 8). In most (but not all) observations, the leading peak is stronger than the trailing peak. Our short 5 minute timing observations do not allow us to determine whether profile variations in the double-peak mode are caused by self-noise in the pulsar-emission mechanism (Kulkarni 1989; Gwinn et al. 2011; Johnson & Gwinn 2012) or if they are associated with distinct magnetospheric states with different period derivatives. The lack of a coherent timing solution further prevents us from comparing the pulsar rotation phase of the emission, which could have provided the means for determining whether the dissimilarities in profile shapes between the emission modes

³⁶ See also www.physics.mcgill.ca/~pulsar/magnetar/main.html.

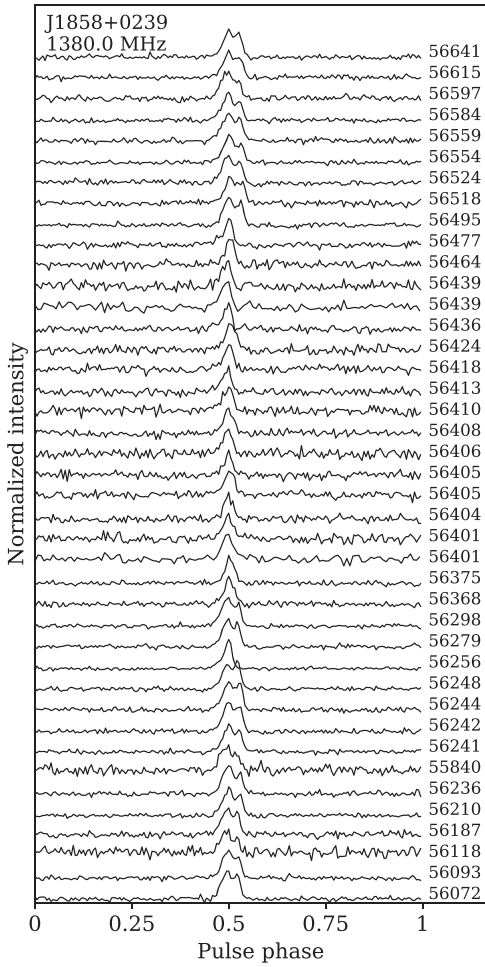


Figure 8. PSR J1858+0239 average pulse profiles. All data presented here were collected with Arecibo. Because we do not have a phase-connected ephemeris for this source, the profiles are not phase aligned but simply have their largest-amplitude peak centered at pulse phase 0.5. Profiles are stacked in chronological order, with the MJD listed on the left of each profile. Partial coherence was achieved for TOAs extracted for MJDs between 56401 and 56439.

are due to jitter or if they are more likely linked to changes in the configuration of the radio beam.

In addition, during one observation (MJD 56186) we observed the pulsar emitting in the bright, double-peak mode ($S_{1400} \approx 143 \mu\text{Jy}$) for the first half of the observation before transitioning to a nulling state (see Section 4.2), where emission was off for the remaining half of the scan (no detectable emission above $\sim 15 \mu\text{Jy}$). van Leeuwen et al. (2002) found that PSR B0809+74 emits in a distinct mode following null episodes. In our case, however, the observation on MJD 56186 unfortunately ended before pulses could be detected again, and the following observation was carried out only three weeks later, at which point the pulse profile was double peaked. Thus, we are not in a position to examine the immediate impact of the nulling episode on the pulsed emission. Yet, the presence of nulling in PSR J1858+0239 demonstrates that magnetospheric state transitions are taking place.

As mentioned earlier, in Section 3.1, we have been unable to produce a fully coherent timing solution for PSR J1858+0239. The potentially large \dot{P} , suggesting a relatively young characteristic age ($\sim 10^5$ yr), and possibly glitch activity could explain why phase connection could not be achieved. Another

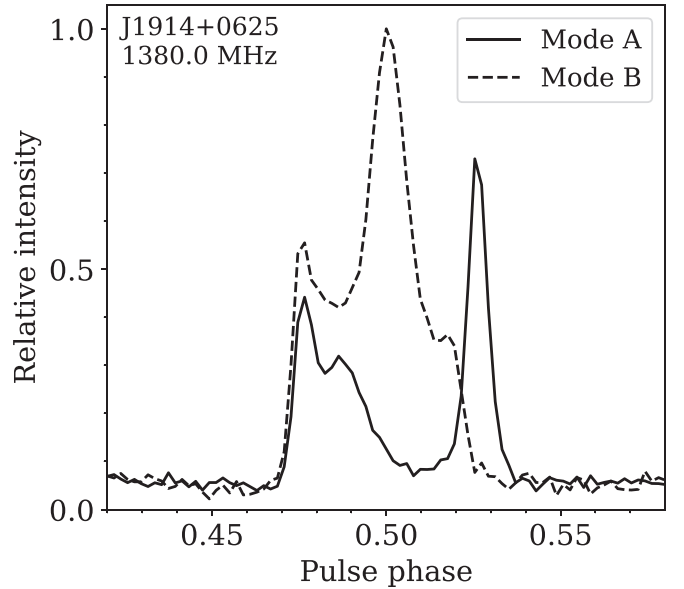


Figure 9. Phase-aligned pulse profiles of the two modes displayed by PSR J1914+0625, calibrated based on their relative fluxes. The data used to generate these integrated profiles were collected with the L-Wide backend at Arecibo.

possibility is that the changes in the pulsar magnetosphere causing the mode-changing and nulling behavior also affect the torque on the NS, which would be detectable as variations in the pulsar period derivative. Correlations between average pulse profiles and spin-down rate have been reported in a number of pulsars (e.g., Lyne et al. 2010; Camilo et al. 2012; Lorimer et al. 2012; Lyne et al. 2017a; Stairs et al. 2019), the most notable being PSR B1931+24, for which weeks-long nulls are associated with a 50% decrease in \dot{P} (Kramer et al. 2006). We note that the two aforementioned possible explanations are not mutually exclusive: Weltevrede et al. (2011) showed that intermittent and erratic emission events in PSR J1119–6127 were preceded by a large amplitude glitch, whereas timing observations of PSR B1828–11 revealed glitch activity (Espinoza et al. 2011) in addition to variations in spin-down rate correlated with observed pulse shape (Stairs et al. 2000, 2019). Interestingly, the latter is a relatively young pulsar ($\tau_c \sim 110$ kyr) whose emission switches between a narrow and brighter profile and a wide and fainter profile (Stairs et al. 2000, 2019). This is similar to what we observed in PSR J1858+0239, but, contrarily to PSR B1828–11, the former’s narrow profile mode is associated with fainter emission. PSR J1858+0239 is thus an interesting object for future studies of physical processes at play in pulsar magnetospheres, the origin of mechanisms that trigger emission state transitions and their impact on timing behaviors.

4.1.3. PSR J1914+0625

Rankin (1993) suggested an empirical classification for radio pulsar pulse profiles that is based on a core/cone emission model. In this model, the radio beam consists of a central core component with nested pairs of conal emission. The intensity and phase separation of components of an observed integrated profile depend on the sightline traverse geometry and the intrinsic shape of the emission beam. Following that classification scheme, PSR J1914+0625 ($P = 0.879$ s) has a five-component (class M) average pulse profile, where pairs of

inner and outer conal emission surround a core component. We observe two distinct emission modes in the integrated profiles, each exhibiting three of the five components. Figure 9 shows the phase-aligned pulse profile of both modes and their relative intensity.

In $\sim 90\%$ of our observations, the pulsar emitted radiation in the normal mode (mode A, plotted with a solid line in Figure 9). Mode A is characterized by emission in both the leading and trailing components of the outer cone, which are separated by 17.6° in pulse longitude, where the leading peak intensity is roughly 60% that of the trailing peak. There is also fainter emission in the leading inner cone, which is $\sim 3.5^\circ$ from the leading outer cone in longitude, and there is no discernible core structure. Only the trailing cone is resolved at 50% level of peak intensity, and the corresponding width (W_{50}) we measure is 6.2 ms. The width at 10% of the peak intensity (W_{10}) for the entire profile in mode A is 56.2 ms, and the average pulsed flux density $S_{1400} = 52 \mu\text{Jy}$.

The brightest configuration is the abnormal mode (mode B), where the strongest emission originates from the core component. The early part of the profile in mode B is illuminated, but the core and the two leading conal components are unresolved. Therefore we do not know whether the inner conal emission is active in this mode. The amount of energy coming from the trailing inner cone in mode B is similar to that of the inner leading cone in mode A, but there is no detectable emission from the trailing outer cone. In mode B, the core is separated by 8.4° from the leading outer cone and by 6.3° from the trailing inner core. The core has a peak width at half-maximum $W_{50} = 14.2$ ms and it is the only resolved structure at that intensity level. The entire emission of the mode B profile has a width $W_{10} = 48.3$ ms and $S_{1400} = 94 \mu\text{Jy}$.

Individual pulses are too faint to investigate potential pulse nulling or subpulse drifting. No transition has been observed within one of our 900 s timing observations (all carried out with Arecibo), implying that both modal emissions are stable on timescales longer than 900 s. Polarization data is unavailable for this source as timing data were only recorded in total intensity mode.

4.2. Nulling Pulsars

First reported by Backer (1970b), the nulling phenomenon is a sudden cessation of detectable pulsed emission that lasts for one or more pulsar cycles. RRATs and intermittent pulsars (discussed in the next sections) are extreme manifestations of pulsar nulling. The triggering mechanism responsible for nulling remains largely unknown, but it is believed to be intimately related with mode changing (e.g., van Leeuwen et al. 2002; Redman et al. 2005; Wang et al. 2007). In general terms, most interpretations of the absence of emission in nulling pulsars invoke processes occurring in the magnetosphere, for example a loss of plasma conditions required for coherent emission (Filippenko & Radhakrishnan 1982), or intense time-varying pulse modulations where the radio flux density drops below the detection threshold (e.g., Esamdin et al. 2005).

Nulling behavior has been reported in approximately 10% of the radio pulsar population, but the proportion of pulsars experiencing nulling could be much larger since most known pulsars are not monitored regularly for the purpose of identifying and studying nulling behavior. For instance, through regular monitoring with CHIME/Pulsar, Ng et al. (2020) recently

reported on the first detections of nulls from bright pulsars discovered decades ago, suggesting that nulling is a phenomenon much more common than previously thought. On the other hand, misinterpreting undetectable emission in data from a given (sensitivity-limited) instrument as a null, as opposed to an extrinsic reduction in the radio flux density (e.g., due to a reduction in intrinsic luminosity or due to scintillation), results in an overestimation of the size of this subpopulation.

Among the pulsars presented in this work, we identify 12 pulsars that displayed discernible nulls. We show examples of the emission intensity as a function of time in Arecibo observations for each pulsar in Figure 10. Because of the low flux densities of these pulsars, data had to be folded into subintegrations ranging from two to ~ 20 pulsar cycles in length. Only the RRAT, PSR J1928+1725 (whose properties are described separately in Section 4.4), has individual pulses with S/N sufficiently high that averaging over multiple rotation is not required.

Dedicated observations with long integrations are preferable for characterizing nulling properties such as nulling fractions and average duration of nulling episodes. This is especially important for pulsars showing long nulling episodes. Such observations were not carried out for this work; all the pulsars here were observed through the same follow-up program at the AO for timing purposes, with scan duration ranging from 5 to 15 minutes. Thus, we do not attempt to determine nulling parameters, except for RRAT J1928+1725, which we discuss in Section 4.4.

4.3. Intermittent Pulsars

While the distribution of nulling fractions in intermittent pulsars can be similar to that in nulling pulsars (e.g., Gajjar et al. 2012), the cessation of pulsed emission in intermittent pulsars is seen on timescales lasting from days to years (e.g., Kramer et al. 2006; Lyne et al. 2017a), orders of magnitude longer than nulling pulsars. Below we discuss the properties of two intermittent pulsars identified in our sample: PSRs J1855+0626 and J1925+2513.

4.3.1. PSR J1855+0626

PSR J1855+0626 ($P = 528.8$ ms) was discovered in 2018 May survey data as a relatively bright pulsar ($S_{1400} = 130 \mu\text{Jy}$) exhibiting short (average duration ~ 16 rotations) but frequent (nulling fraction of $\sim 39\%$) nulling episodes. From the time of discovery until 2020 August, we carried out 36 300 s follow-up observations of the pulsar at the AO, for a total of 3 hr. The pulsar was only redetected once; it was in a quiescent state the rest of the time (upper limit $S_{1400} \lesssim 12 \mu\text{Jy}$). An extensive follow-up campaign was also carried out at the JBO. A total of 148 30 minute observations at JBO between 2019 November and 2021 March led to only two detections of the pulsar. Hence PSR J1855+0626 was inactive in 98.4% of our observations. The top panel of Figure 11 shows the timeline of the observations, and epochs where the pulsar was active are highlighted in blue.

In 2020 June, we began observing PSR J1855+0626 with CHIME/Pulsar on a regular basis, but to date we have not been able to detect the pulsar. We note, however, that it is possible that radio pulsations were being emitted during an observation but that their flux density in the CHIME band was below the

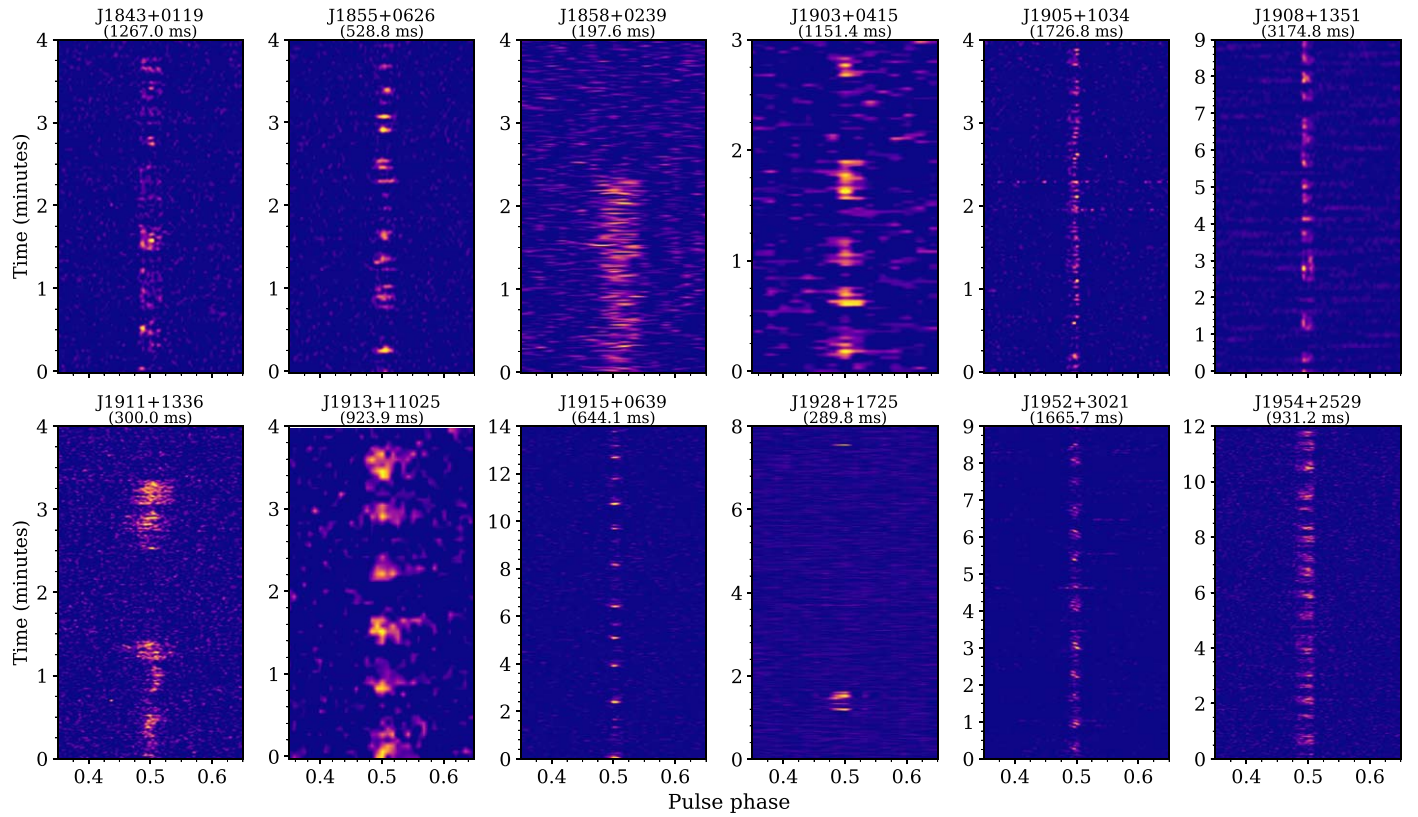


Figure 10. Phase–time plots showing the variation in intensity at 1.4 GHz in single Arecibo observations for the 12 pulsars that display nulling behavior.

instrument sensitivity. Due to the rarity of detections, we do not have a phase-coherent timing solution for PSR J1855+0626.

4.3.2. PSR J1952+2513

We have observed PSR J1952+2513 ($P = 1077.6$ ms) for a total of 2.6 hr with AO in 2012 and 2013 (26 sessions). The pulsar was observed in an active state in 39% of our observations. With an average pulsed flux density of only $36 \mu\text{Jy}$, the pulsar is one of the faintest in our sample. In some of the follow-up data, measured S_{1400} values have been as low as $\sim 15 \mu\text{Jy}$, near the sensitivity limit for most of our timing observations at the AO. These variations are not caused by diffractive scintillation—the DM (246.9 pc cm^{-3}) of the pulsar is too large for that—but instead caused by variations in the telescope sensitivity and the RFI environment, which may have hindered our ability to identify weak emission during what we considered inactive states. Thus, it is possible that we are overestimating the fractional time spent in the inactive state. Another consequence of the low brightness of PSR J1952+2513 is that, unlike PSR J1855+0626, we are unable to identify and characterize potential nulling behaviors when the pulsar is active.

One interesting feature of this pulsar is that, if it is indeed an intermittent pulsar, its \dot{P} is one order of magnitude smaller than expected from the observed relation between P and \dot{P} for other intermittent pulsars by Lyne et al. (2017a) (see their Figure 7). That relation suggested that all intermittent pulsars have the same spin-down energy and the same acceleration potential above their polar caps. Thus, PSR J1952+2513 might be indicating that intermittent pulsars have a wider distribution of spin-down energies than previously recognized.

4.4. RRAT J1928+1725

PSR J1928+1725 ($P = 289.8$ ms) is a RRAT that emits bright, heavily clustered pulses followed by long (hundreds of rotations) nulls. Other than the single pulses themselves, no underlying signal is visible when folding the data. We analyzed the distribution of wait times between consecutive pulses, and find that this distribution is inconsistent with a Poisson process (see Figure 12). The longest active phase we observe lasts 29 consecutive pulsar cycles, while the longest inactive phase lasts 1662 cycles (~ 482 s). Active phases are also rare: we detect neither single-pulse or periodic emission in three/17 of our 15 minute observations of PSR J1928+1725. The average detection rate is 78 pulses per hour.

Despite having detected numerous bright pulses, the long time gaps between observations during which pulses are detected makes it difficult to maintain timing coherence over a few epochs, and thus we have been unable to solve this RRAT. PSR J1928+1725 could be similar to the young and energetic ($\tau_c = 865$ kyr and $\dot{E} = 4.6 \times 10^{34} \text{ erg s}^{-1}$) 125 ms PSR J1554–5209 (Keane et al. 2010), one of the very few RRATs having a spin period < 500 ms for which \dot{P} has been measured.³⁷ Keane et al. (2011) conducted a timing analysis on PSR J1554–5209 along with a dozen more RRATs with longer periods and lower \dot{E} , and noted that PSR J1554–5209 displays a far larger scatter in its timing residuals than the other, lower- \dot{E} RRATs. Significant jitter in pulse phase similar to PSR J1554–5209 could explain why we have been unable to derive a coherent timing ephemeris for PSR J1928+1725. During our phase-connection attempt, it also appeared that the pulsar may be suffering from significant glitch activity, although we cannot

³⁷ Based on the ATNF catalog, Manchester et al. (2005).

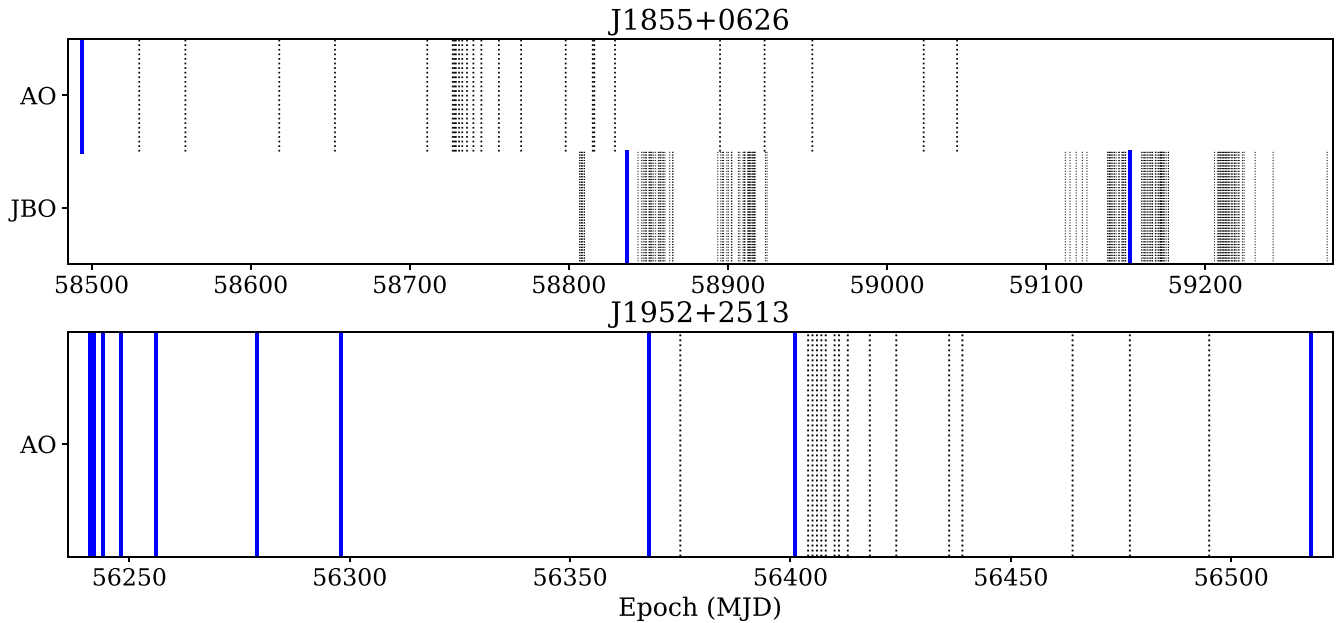


Figure 11. Epoch of observations where pulsations were detected (solid blue) and were not detected (dotted black) in observations of PSRs J1855+0626 (top) and J1952+2513 (bottom). For PSR J1855+0626, AO and JBO data sets are shown on the upper and lower rows, respectively. PSR J1952+2513 was observed at the AO exclusively.

confirm this. Of the 34 known RRATs with reported spin-down rate measurements (Manchester et al. 2005), PSR J1819–1458 (McLaughlin et al. 2006) is the only one for which glitch activity has been reported (Bhattacharyya et al. 2018). While the former has a much longer rotation period ($P = 4.263$ s) than PSR J1928+1725, it has a relatively small characteristic age of 120 kyr. If PSR J1928+1725 is indeed young and energetic, the presence of glitches could very well explain why we have been unable to solve it. Follow-up observations of PSR J1928+1725 were carried out with CHIME/Pulsar from 2020 October to 2021 April, but no pulses were detected. Establishing phase coherence would require regular and long-integration observations with an instrument whose sensitivity is similar to that of Arecibo.

4.5. Glitching Pulsars

Rotational instabilities in pulsars are generally explained by either timing noise or glitches. Whereas timing noise arises from random spin fluctuations over long timescales (e.g., one of our pulsars, PSR J0608+1635, displays intense timing noise; see residuals in Figure 3), a glitch is a discrete transition in the pulsar rotational state marked by an abrupt increase in spin frequency, typically with frequency jump magnitudes between $10^{-6}\nu$ and $10^{-10}\nu$, and often accompanied by a decrease in frequency derivative $\dot{\nu}$ (Espinoza et al. 2011). Glitches are believed to be caused by erratic transfers of angular momentum from the superfluid inside the star to the more slowly rotating (and cooling) crust (Anderson & Itoh 1975; Ruderman et al. 1998). Hence their study represents a unique opportunity to gain insight into the internal structure of NSs.

Eight glitches of moderate and small magnitude were detected in five of the 72 pulsars presented here during the timing program. Figure 13 illustrates the glitch signatures in timing residuals when they are not included in the timing model, signatures that are characterized by the sudden onset of a steady decrease toward negative residuals. We are able to

maintain phase coherence over the time gap between observations around the glitch epochs when using the best-fit glitch parameters listed in Table 6 in our timing models. Residuals corresponding to the ephemerides that contain the best-fit glitch parameters are the ones shown in Figure 3. As a result of sparse observation cadences and/or high levels of timing noise and/or large TOA uncertainties, we are unable to detect the changes in the spin-down rate ($\Delta\nu$) during recovery for three glitch events.

The three youngest pulsars presented in this work, PSRs J1910+1026 ($\tau_c = 33$ kyr), J1931+1817 ($\tau_c = 35$ kyr), and J1915+1150 ($\tau_c = 116$ kyr), have all exhibited glitch activity. This is not surprising, as young pulsars are known to display higher glitch activity (e.g., McKenna & Lyne 1990; Lyne et al. 2000; Janssen & Stappers 2006; Espinoza et al. 2011).

The largest glitch we observed occurred in PSR J1910+1026, the youngest pulsar in our set, with a fractional step in spin frequency of $78.4 \pm 0.8 \times 10^{-9}\nu$. Due to its low flux density (58 μ Jy at 1.4 GHz), timing data were solely collected with Arecibo and the pulsar was observed roughly twice a month for ~ 1.5 yr. The sparse observations combined with the relatively large timing residuals (~ 1 ms) makes the identification of smaller glitches difficult. For the aforementioned reasons, the glitch activity of PSR J1910+1026 is not well constrained and could be much higher than what our data set reveals.

On the other hand, PSRs J1931+1817, J1939+2609, and J1954+2529 were bright enough to be followed up at the JBO and CHIME/Pulsar, and benefited from more regular timing observations over a longer time span. Over the course of our 5 yr follow-up campaign of PSR J1931+1817, we detected four glitches ranging from 3.3×10^{-10} to $3.7 \times 10^{-8}\nu$ in size. A small glitch ($\Delta\nu/\nu = 6.0 \times 10^{-10}$) was observed in PSR J1954+2529, a relatively old ($\tau_c = 11.7$ Myr) nonrecycled pulsar in a binary system, which we discuss in Section 4.7.

Even more surprising is that PSR J1939+2609, an old pulsar with characteristic age $\tau_c \sim 1.4$ Gyr, suffered a glitch, albeit

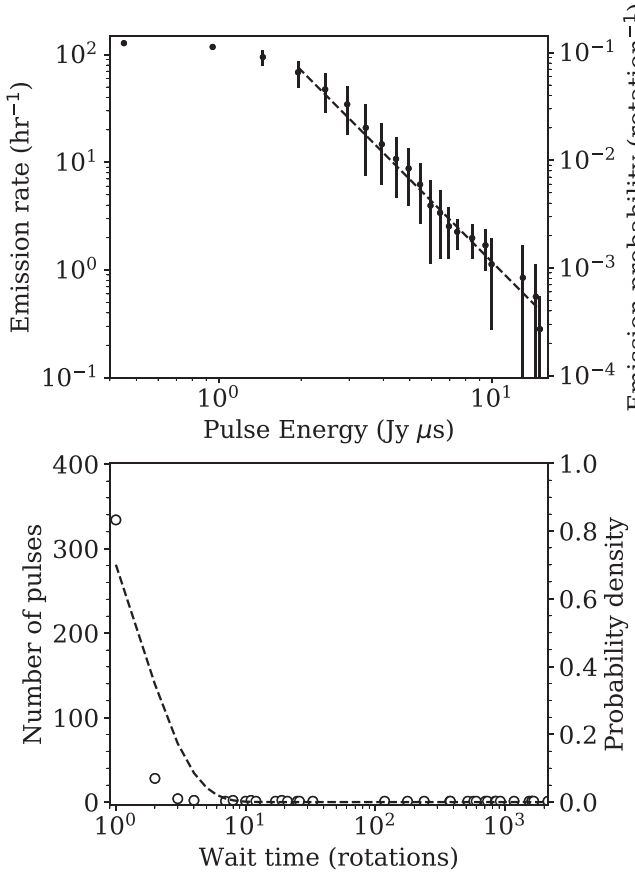


Figure 12. Single-pulse statistics for RRAT J1928+1725. Top: cumulative emission rate and emission probability of single pulses exceeding a given pulse energy, binned in intervals of $0.5 \text{ Jy } \mu\text{s}$. The dashed line shows the power law that best fits the pulse energy distribution, which has an index of $-2.6(2)$. Bottom: distribution of wait times between consecutive single pulse detections, which shows that during the short, bright episodes where the RRAT is active, most detectable pulses are emitted consecutively or within very few rotations of the pulsar. The dotted curve is an exponential fit to the wait-times distribution, i.e., the expected distribution if the emission of pulses is a Poisson process. The emission mechanism responsible for RRAT J1928+1725’s bright single pulses produces pulses that are more clustered than a Poisson process.

of small magnitude, $3.3 \times 10^{-10} \nu$. Only two other glitching pulsars with ages $>100 \text{ Myr}$ are known in the Galactic field: PSRs B1913+16, with $P = 59 \text{ ms}$ and $\tau_c = 109 \text{ Myr}$ (Hulse & Taylor 1975), and J0613–0200, a 3.1 ms MSP with $\tau_c = 5 \text{ Gyr}$ (Lorimer et al. 1995). Similar to PSR J1939+2609, only one glitch of small magnitude has been detected in each system, with $\Delta\nu/\nu = 3.7 \times 10^{-11}$ for PSR B1913+16 (Weisberg et al. 2010; Weisberg & Huang 2016) and 2.5×10^{-11} for PSR J0613–0200 (McKee et al. 2016).

We note, however, that for PSRs J1939+2609, J1954+2529, and J1931+1817 (first glitch; MJD 57645), we cannot positively rule out the possibility that the features in the timing residuals are caused by timing noise rather than glitch activity. While the latter explanation minimizes the postfit rms residuals in these systems and is thus currently preferred over the former, future modeling of their long-term timing behavior will be needed to be certain that those are real glitches and not part of large timing noise features.

4.6. Young Pulsars

Among the 69 pulsars with coherent timing solutions, only two are young ($\tau_c < 10^5 \text{ yr}$) objects: PSRs J1910+1026

($P = 531.5 \text{ ms}$) and J1931+1817 ($P = 234.1 \text{ ms}$), with characteristic ages of 33 and 35 kyr, respectively. Pulsars of such young age are often found in supernova remnants (SNRs). Despite the lack of proper motion measurements—important to confirm any potential pulsar/remnant association—we searched for coincident SNRs by cross-matching the pulsar positions against Green’s SNR Catalog (Green 2019). Accounting for potential angular offsets that could arise from large postsupernova tangential velocities, we search over a conservative region of 0.5° radius around each pulsar. No remnant coincident with PSR J1910+1026 was identified, which is not surprising given its very large inferred distance ($\gtrsim 15 \text{ kpc}$). One cataloged object, SNR G53.41+0.03 (Anderson et al. 2017), is found $28'$ away from the timing position of PSR J1931+1817. Driessen et al. (2018) carried out a deep radio search for a pulsar associated with G53.41+0.03, covering a $10'$ region around the center of the SNR (the estimated size of the remnant), but did not detect pulsations. They also investigated and characterized G53.41+0.03 using multiwavelength data, and estimated its distance at roughly 7.5 kpc and its age at ~ 1000 to 8000 yr . Given the $28'$ angular offset and adopting a distance of 7.5 kpc and the most conservative age of 8000 yr , an unreasonably high spatial velocity ($> 12 \times 10^3 \text{ km s}^{-1}$) would be required for PSR J1931+1817 to have traveled from its birth location near the center of the remnant to its current position. We therefore rule out SNR G53.41+0.03 as being associated with PSR J1931+1817.

Due to their large spin-down power, \dot{E} , young pulsars sometimes have high-energy counterparts. However, we did not find any gamma-ray point sources or pulsations in Fermi Large Area Telescope (LAT) data for these pulsars (analysis described in Section 5). This is also not surprising given the large distances of the pulsars and the corresponding “heuristic” energy fluxes $\sqrt{\dot{E}/d^2}$ of $\sim 3 \times 10^{15}$ and $\sim 5 \times 10^{15} (\text{erg s}^{-1})^{1/2} \text{ kpc}^2$ for PSRs J1910+1026 and J1931+1817, respectively, below the approximate LAT threshold of $10^{16} (\text{erg s}^{-1})^{1/2} \text{ kpc}^2$ (Abdo et al. 2013; Smith et al. 2019).

4.7. An Unusual Binary System: PSR J1954+2529

Of all the new pulsars presented here, only one, PSR J1954+2529, is a member of a binary system. It has an orbital period of 82.7 days and, interestingly, a system eccentricity of 0.11. The system has been monitored with Arecibo and CHIME, but mostly with the Lovell telescope. PSR J1954+2529 is also among our five pulsars that displayed a glitch. The Keplerian parameters of the pulsar’s orbit and some derived quantities are presented in Table 7. Included in our timing model is the relativistic advance of the angle of periastron, $\dot{\omega}$, which in GR is a function of the total mass of the system, M_{tot} . Unfortunately our timing data do not yet provide a significant measurement (see upper limit in Table 7), and the 3σ upper limit on $\dot{\omega}$ does not yield a meaningful constraint on M_{tot} .

The pulsar does not appear to be recycled: with $P = 0.931 \text{ s}$, a characteristic age of about 12 Myr and a magnetic field at the surface of about 10^{12} G , it is near the center of the cloud of “young” pulsars in the $P-\dot{P}$ diagram (see Figure 6). Such middle-aged radio pulsars in binary systems are rare but interesting from the point of view of stellar evolution.

In what follows, we discuss three possibilities for the formation and nature of this system. At the moment, we have no data to decide in favor of any hypothesis, but the last

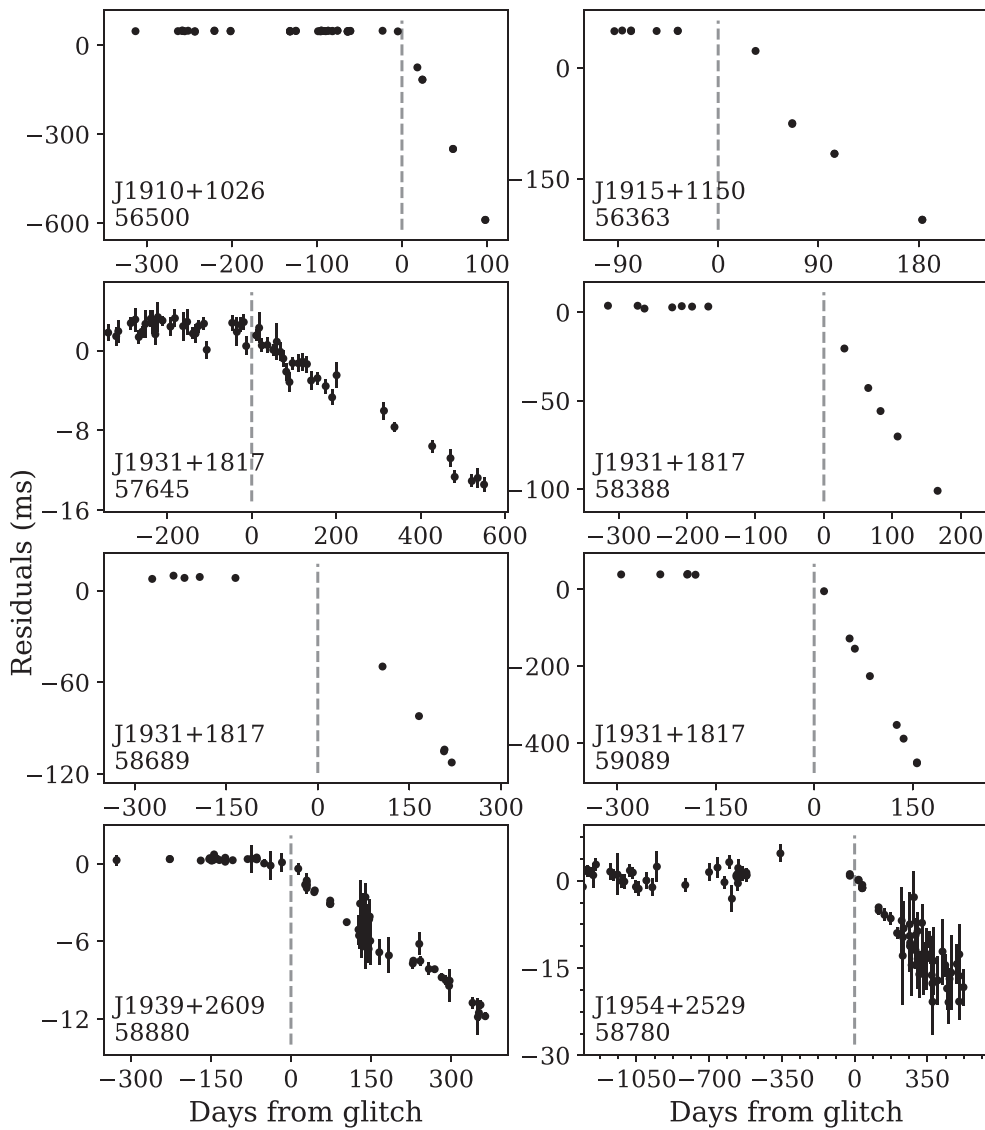


Figure 13. Glitch detections in the five pulsars exhibiting glitch activity, showing the residuals obtained when not fitting for glitch parameters (Table 6) from the timing model and keeping best-fit rotation and position parameters fixed (Table 3). Residuals for the four glitches detected in PSR J1931+1817 are shown separately, each time by using a timing solution that includes all glitch parameters (fixed) and excluding only the ones associated with the glitch being displayed. Best estimates for the MJD of the glitch epochs are listed below the pulsar name in each panel.

hypothesis is currently preferred based on theoretical arguments from stellar evolution theory.

4.7.1. A Progenitor to a Low-mass X-ray Binary

Although most massive stars that eventually form pulsars are born in binary systems (e.g., Abt 1983; Duchêne et al. 2001; Sana & Evans 2011), when one of the stars in these systems (generally the most massive) undergoes a supernova (SN), they will in most cases become unbound. This is why, among normal pulsars, isolated pulsars are hundreds of times more prevalent than binaries.

Systems that survive the first SN will consist of a young pulsar in an eccentric orbit with a bright, massive main sequence (MS) star. There are six such systems in the literature, all with massive companions; they are listed in Table 8. The orbits of most of these systems are quite unlike that of PSR J1954+2529; not only are their eccentricities much higher ($e > 0.5$)—so high in some cases that they suggest near-

disruption of the system—but their companions are much more massive ($M_c > 5 M_\odot$).

If the companion to PSR J1954+2529 is a MS star, it has to be much less massive (consistent with the system's mass function), and therefore much cooler, consistent with the nondetection of an optical counterpart. An examination of existing point-source catalogs revealed no point source within $5''$ of the position of the pulsar, which has only a $0.15''$ uncertainty. The DM-estimated distance of PSR J1954+2529 is 6.8 and 7.8 kpc for the NE2001 and YMW16 models, respectively. The magnitude limits for a 10σ detection in the 2MASS point-source catalog are 15.8, 15.1 and 14.4 for the J , H and K bands, respectively (Skrutskie et al. 2006). We use this survey because these near-infrared bands are least affected by reddening, up to 2.33, 1.484 and 1.000 magnitudes of absorption in these bands (Schlafly & Finkbeiner 2011).³⁸

³⁸ <https://irsa.ipac.caltech.edu/applications/DUST/>

Table 6
Glitch Parameters for the Five Pulsars that Displayed Glitch Activity

PSR (J2000)	Glitch No.	Epoch (MJD)	$\Delta\nu/\nu$ (10^{-9})	$\Delta\dot{\nu}/\dot{\nu}$ (10^{-3})
J1910+1026	1	56500(2)	78.4(8)	1.6(3)
J1915+1150	1	56363(4)	29.19(7)	-20.51(7)
J1931+1817	1	57645(9)	0.314(9)	—
	2	58388(2)	8.8(3)	0.49(7)
	3	58689(6)	6.3(7)	—
	4	59089(2)	36.5(7)	0.22(9)
J1939+2609	1	58880(2)	0.333(3)	—
J1954+2529	1	58780(9)	0.61(5)	7(2)

Note. For each glitch, we list its epoch and the fractional change in spin frequency $\Delta\nu/\nu$ and in frequency derivative $\Delta\dot{\nu}/\dot{\nu}$. Numbers in parentheses are the 1σ uncertainties on the last digit reported by TEMPO after weighting the TOAs such that $\chi^2 = 1$.

Given the pulsar’s distance estimates, the 2MASS magnitude limit, and the lack of a detected point source at the pulsar position, a MS companion to PSR J1954+2529 must have a mass smaller than $2 M_{\odot}$ and therefore a spectral type later than F0.

The problem with such an identification is that no such systems have been otherwise identified: all MS companions to unrecycled pulsars are quite massive. However, such systems should exist, because they are the theoretical progenitors to low-mass X-ray binaries (LMXBs). The hypothesis of a MS companion can be investigated further via deeper optical observations of the position of the system.

4.7.2. Is the Pulsar the Younger Degenerate Object in the System?

Most known binary pulsars evolve as MSPs: following one (or more) episode of mass transfer, the NS is spun up to short spin periods and the orbit is circularized. If the donor has a low mass, it evolves into a white dwarf (WD). This clearly does not describe the evolution of PSR J1954+2529. However, if the donor is massive enough, it may undergo a SN and become a NS, possibly causing the orbit to be eccentric again. The companion would then be observed as a young pulsar.

The only confirmed case of a young pulsar observed in a double-NS (DNSS) system is that of PSR J0737–3039B, the second pulsar of the double-pulsar system (Lyne et al. 2004). There are other candidates, like the young pulsars J1906+0746, the first binary system found in the PALFA survey (Lorimer et al. 2006b; van Leeuwen et al. 2015), and J1755–2550 (Ng et al. 2018). However, no pulsations from a recycled pulsar companion were detected in either system. For PSR J1954+2529, we obtained several long observations in search mode with the Arecibo telescope. Because of heavy RFI, only three proved usable, with integration lengths of 16, 30 and 30 minutes. Dedispersing the data from these observations at the DM of PSR J1954+2529, and then doing a simple Fourier transform (no acceleration is expected given the long orbital period) did not reveal any other radio pulsars in the same observations. Assuming, conservatively, a minimum S/N of 10, we can derive, based on the radiometer equation, upper limits for the flux density of the companion as a function of the assumed pulse duty cycle. These are presented in Figure 14. At the assumed distance of 7.6 kpc, these translate (assuming a pulse duty cycle of 5%) to a pseudoluminosity of $\sim 0.45 \text{ mJy kpc}^2$, placing it within the bottom 7.5% of all radio

Table 7
PSR J1954+2529’s Keplerian Orbital Parameters

Orbital Parameters	
Binary model	DD
Orbital period, P_b (d)	82.71733(5)
Proj. semimajor axis, $x = a \sin i/c$ (lt-s)	71.62485(9)
Time of periastron, T_0 (MJD)	58094.3699(6)
Eccentricity, e	0.114023(3)
Longitude of periastron, ω (deg)	78.545(2)
Derived Parameters	
Mass function (M_{\odot})	0.0576608(2)
Minimum companion mass (M_{\odot})	0.62
Median companion mass (M_{\odot})	0.74
Advance of periastron, $\dot{\omega}$ (deg/yr)	<0.003

Note. Numbers in parentheses are TEMPO-reported uncertainties in the last digit quoted. Minimum and median companion masses are calculated assuming a pulsar mass of $1.4 M_{\odot}$. We also provide the 3σ upper limit on the relativistic advance of periastron produced by our timing model.

pulsars with reported pseudoluminiosities at 1400 MHz in the ATNF pulsar catalog. This does not by itself exclude the possibility of a DNS system—the first pulsar could be pointed away from our line of sight, or it could just be very faint—but does not support it either.

The older degenerate objects in the PSR J1906+0746 and PSR J1755–2550 systems can alternatively be massive WDs, as in the case of PSR B2303+46 (Thorsett et al. 1993; van Kerkwijk & Kulkarni 1999). The formation and evolution of these systems from nearly equal-mass MS binaries is described in detail by Tauris & Sennels (2000), who predicted that PSR J1141–6545 (Kaspi et al. 2000) also has a massive WD companion. This was confirmed by the measurement of the companion mass, $1.02 \pm 0.01 M_{\odot}$ (Bhat et al. 2008) and by optical observations (Antoniadis et al. 2011). The detailed evolution of the system was finally proven when the companion WD showed clear signs of having been spun up by accretion of mass from the progenitor of the pulsar (Venkatraman Krishnan et al. 2020). One apparent advantage of this hypothesis is that the companion mass estimates of PSR J1954+2529 are, indeed, in better agreement with the possibility of a massive WD.

Let us look in more detail into this possibility. During the giant phase of the pulsar progenitor, there was likely mass transfer to the companion of PSR J1954+2529, whether a WD or NS. This would have circularized the orbit. After the SN, the mass loss and kick would greatly increase the orbital eccentricity, to values that are, as we will see below, likely much higher than 0.11. However, it is possible the PSR J1954+2529 formed in an electron-capture supernova (ECSNe), which could in principle occur for companions with initial masses near $8 M_{\odot}$. If these are perfectly symmetric, with no associated kick, then the post-SN eccentricity will be given by Equation (20) of Tauris et al. (2017):

$$e = \frac{\Delta M}{M_T}, \quad (1)$$

where ΔM would be the mass loss during the SN (which includes the binding energy of the NS) and M_T is the total mass of the system after the SN. For the double-pulsar system, we know the second SN had a kick between 0 and 50 km s^{-1} ,

Table 8
Comparison Between the Pulsars with Massive Main Sequence (MS) Companions and Systems Similar to PSR J1954+2529

Pulsar	P (s)	\dot{P} (10^{-15})	τ_c (Myr)	B (10^{12} G)	P_b (days)	e	Min. M_c (M_\odot)	Mass Function (M_\odot)	Comp.	Ref.
J2032+4127	0.1432	11.3	0.21	1.29	16835	0.964	11.86	9.488	MS	(10,11)
B1259–63	0.0478	2.28	0.33	0.33	1236.7	0.870	3.17	1.529	MS	(2,9)
J1740–3052	0.5703	25.5	0.35	3.86	231.0	0.579	11.07	8.723	MS	(7,8)
J1638–4725	0.7639	4.8	2.53	1.93	1940.9	0.955	5.90	3.852	MS	(6)
B1820–11	0.2798	1.38	3.22	0.63	357.8	0.795	0.66	0.068		(1,5)
J0045–7319	0.9263	4.46	3.29	2.06	51.2	0.808	3.97	2.170	MS	(3,4)
J1954+2529	0.9312	1.26	11.7	1.10	82.7	0.114	0.62	0.058		This work
J1932+1500	1.8643	0.459	64.4	0.94	198.9	0.029	0.33	0.012		(12)
J1822–0848	0.8348	0.135	97.7	0.34	286.8	0.059	0.33	0.012		(6)
J1837–0822	1.0992	0.121	144	0.37	98.4	0.024	0.28	0.008		(13)

Note. Pulsars have been ordered by increasing characteristic age (τ_c). Minimum companion masses, M_c , assume a pulsar mass of $1.4 M_\odot$. References listed in the last column are, by order of publication: (1) Lyne & McKenna (1989), (2) Johnston et al. (1994), (3) Bell et al. (1995), (4) Kaspi et al. (1996), (5) Hobbs et al. (2004), (6) Lorimer et al. (2006a), (7) Bassa et al. (2011), (8) Madsen et al. (2012), (9) Shannon et al. (2014), (10) Lyne et al. (2015), (11) Ho et al. (2017), (12) Lyne et al. (2017b), (13) Burgay et al. (2019). Values for PSR J1954+2529 are from this work. All low-eccentricity systems similar to PSR J1954+2529 are older than pulsars with MS companions, their magnetic fields are only slightly smaller.

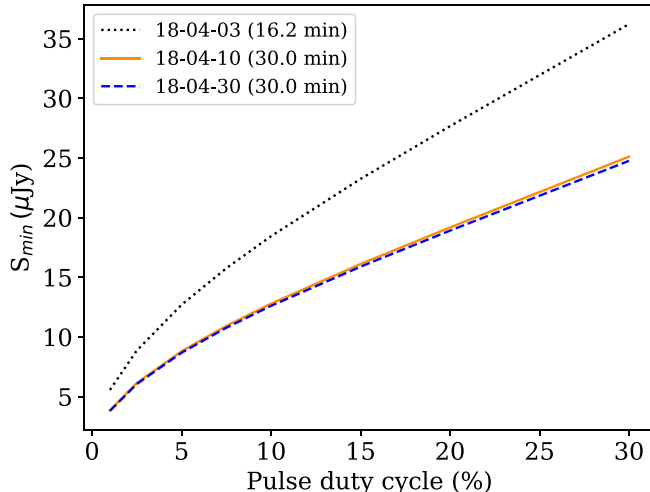


Figure 14. Upper limits for the flux density at 1.4 GHz of a possible radio pulsar companion to PSR J1954+2529.

which is small compared to the orbital velocities in that system, thus without significant effect on the eccentricity or even the orbital inclination of the system (Ferdman et al. 2013; see discussion in Tauris et al. 2017 and references therein). This means that we can estimate the mass loss associated with the second SN: it was such that the post-SN eccentricity was ~ 0.1 . This is similar to what we observe for PSR J1954+2529.

However, the problem for PSR J1954+2529 is that it has a much wider orbit. Extensive simulations carried out by Ng et al. (2018) and Kruckow et al. (2018) show very few binaries with $e < 0.5$ for orbital periods of 80 days or larger (see their Figure 7). The reasons for this are twofold: first, for more widely separated binaries, mass stripping, which determines in these simulations the kick magnitude for iron-core-collapse SNe, is less effective, and the larger envelopes result in larger kicks. Second, the simulation also includes an ECSNe, with kick velocities between 0 and 50 km s^{-1} with a flat probability distribution (Kruckow et al. 2018); these are consistent with the estimates for the second NS in the double pulsar (Tauris et al. 2017). Even such small kicks will, when added to the small orbital velocities of wider systems, significantly raise their

orbital eccentricities. In a few cases where the kicks point nearly 180° away from the orbital motion of the system the resulting orbital eccentricities are low, however such cases are relatively rare. Thus, if one assumes these simulations—and in particular, their assumptions regarding SN kick distribution—faithfully capture reality, then it is highly unlikely, though not impossible, that PSR J1954+2529 is the second degenerate object in the system.

4.7.3. A Nonrecycled Pulsar–Massive White Dwarf System?

A third possibility is discussed in detail by Tauris et al. (2012): as described above, after the SN that formed the first NS, the latter was in an eccentric and wide orbit with its massive MS star companion. The companion then evolves into the asymptotic giant branch, with a weakly bound envelope and a massive stellar wind. These circularize the orbit either partially or, if the orbit is very wide, not at all. These stellar winds will also cause very mild accretion into the pulsar, barely spinning it up. If its initial mass is below $\sim 8 M_\odot$, the companion will eventually evolve into a massive WD. Since the system’s mass loss is slow, there would be no further changes to the orbital eccentricity of the system.

There are four other binary pulsars thought to have formed in this way: three with partially circularized orbits (PSRs J1822–0848, J1837–0822, and J1932+1500, the latter found in PALFA), and one with a wider, eccentric orbit, (PSR B1820–11; see Table 8). The orbital characteristics and B-field of PSR J1954+2529 are similar to those of the three partially circularized systems. Finally, the mass functions for PSR J1954+2529 and B1820–11, and the minimum companion mass estimates derived from them are in good agreement with the possibility of a massive WD companion, and significantly larger than the mass for a He WD predicted for their orbital periods by Tauris & Savonije (1999). This is not the case for the other three partially circularized systems, which have smaller mass functions and minimum masses of about $0.3 M_\odot$; this does not exclude the possibility of massive WD companions, as it could be caused by lower orbital inclinations. From this point of view, PSR J1954+2529 and to some extent PSR B1820–11 provide the best evidence that at least some of these systems are associated with massive WDs.

There is a simple consistency test for this hypothesis. If it is true that the systems similar to PSR J1954+2529 started as PSR–O/B systems, and later evolved to PSR–massive WD systems, then the main difference between them should be, apart from the companion mass and orbital eccentricity, the characteristic age: the systems with O/B companions must be young enough to still have unevolved O/B companions, whereas the systems like J1954+2529 should be older. The magnetic fields of the latter pulsars should be similar, but slightly smaller, not only because of possible minor accretion, but also because of observational biases: larger B-fields cause a larger braking torque, which means that a pulsar will reach the death line sooner. Ordering Table 8 by characteristic age, we see that the results are in agreement with this expectation. Interestingly, PSR B1820–11 is slightly younger than PSR J0045–7319. Assuming that the characteristic age is a close indicator of actual age, this would suggest that the companion of PSR B1820–11 was slightly more massive than the companion of PSR J0045–7319, which made it evolve faster into a massive WD.

B1820–11 and J1954+2529 are the youngest systems within their class. This raises the possibility that, if their companions really are massive WDs, they might still be hot and bright enough for detection in deeper optical observations.

5. Search for Gamma-ray Associations

Where most nonrecycled pulsars have spin-down powers $\dot{E} \gtrsim 10^{34}$ erg s $^{-1}$ (Abdo et al. 2013), gamma-ray pulsations have been found in low- \dot{E} radio pulsars by folding Fermi LAT data using their ephemerides. For instance, Smith et al. (2019) found pulsations in PSR J2208+4056 (Swiggum et al. 2014), a pulsar with $\dot{E} = 8 \times 10^{32}$ erg s $^{-1}$, a spin-down power well below the “death line” for gamma-ray emission (Arons 1996; Abdo et al. 2013; Kalapotharakos et al. 2017). Hence, we search for gamma-ray counterparts to all pulsars presented here.

First, we attempt to identify gamma-ray point sources coincident with our pulsars by cross-matching the Fermi LAT fourth catalog³⁹ of gamma-ray sources (Abdollahi et al. 2020) against the timing positions (or discovery positions, if unsolved) of our 72 pulsars. We find three unidentified Fermi point sources for which the reported semimajor axis of the error ellipse at the 95% confidence level is coincident with our sources and no other known radio pulsars.

The first is 4FGL J1912.0+0927, coinciding with PSR J1911+0925, a pulsar with $\tau_c = 1.4$ Myr and $\dot{E} = 4 \times 10^{33}$ erg s $^{-1}$. The Fermi source was detected at a 7.0σ significance level and has a log-normal spectrum, common in gamma-ray pulsars. NE2001 and YMW16 suggest distances of 6.9 kpc and 8.1 kpc for this pulsar, corresponding to energy fluxes $\sqrt{\dot{E}}/d^2$ of $\sim 1.3 \times 10^{15}$ and $\sim 1.0 \times 10^{15}$ (erg s $^{-1}$) $^{1/2}$ kpc 2 , roughly one order of magnitude below the LAT 10^{16} (erg s $^{-1}$) $^{1/2}$ kpc 2 threshold. However, it is possible that the DM distances are overestimated and thus we cannot rule out the association based on $\sqrt{\dot{E}}/d^2$ alone.

The second possible association is 4FGL J1911.3+1055, a low-significance (4.32σ) point source that has a power-law spectrum, also consistent with gamma-ray pulsar spectra, and a position matching that of PSR J1911+1051, one of our glitching pulsars. That pulsar is relatively young ($\tau_c = 249$ kyr), has a

spin-down power of 7×10^{34} erg s $^{-1}$ and its DM-derived distances are 9.0 and 10.1 kpc for the NE2001 and YMW16 models, respectively, corresponding to low $\sqrt{\dot{E}}/d^2$ values of $\sim 3.3 \times 10^{15}$ and $\sim 2.6 \times 10^{15}$ (erg s $^{-1}$) $^{1/2}$ kpc 2 .

Finally, 4FGL J1929.0+1729 is coincident with the discovery position of our RRAT, PSR J1928+1725 ($P = 289.8$ ms). The detection significance of this Fermi source is $\sigma = 14.8$ and it has a log-normal spectrum. Because we were unable to achieve phase connection for PSR J1928+1725, its age and spin-down power (and thus $\sqrt{\dot{E}}/d^2$) are unknown. As discussed in Section 4.4, we suspect that our inability to solve PSR J1928+1725 is a result of the pulsar being young, energetic, and potentially suffering from glitch activity. It is common for young gamma-ray pulsars to exhibit glitches (e.g., Ray et al. 2011, 2012; Pletsch et al. 2012; Allafort et al. 2013; Gügercinoğlu et al. 2020). Thus 4FGL J1929.0+1729 may indeed be associated with PSR J1928+1725, but this cannot be confirmed without a coherent timing solution.

In an attempt to confirm the potential Fermi point sources associations with PSRs J1911+0925 and J1911+1051, as well as to detect pulsations from any other sources that would not have met the various selection criteria used in constructing the Fermi 4FLG catalog (Abdollahi et al. 2020), we use the timing ephemerides of solved pulsars to fold ~ 11 yr of Fermi LAT data. We extract photons in the energy range 100 Mev $< E_\gamma < 500$ GeV and follow a similar procedure as Smith et al. (2019), but because our pulsars are located in the plane where the background level is high, we use a high energy-scale value $\mu_E = \log_{10}(E_{\text{ref}}/1 \text{ MeV})$ of 4.1 rather than a value closer to ~ 3.6 , which generally fits well most pulsar spectra (Smith et al. 2019). No pulsations were identified from any of our sources above a detection threshold of 5σ , including PSRs J1911+0925 and J1911+1051. We note that nondetections are somewhat anticipated here given that all but three pulsars have inferred distances > 3 kpc and are located in highly confused regions.

6. PALFA and the Galactic Plane Population

Most NSs in the Galactic field lie in the plane; however, the higher background sky temperature and plasma density have hindered pulsar searches in low-latitude regions. One of the primary goals of the PALFA survey had been to probe the true population deep in the Galactic plane in order to disentangle the spatial distribution and ISM from pulsar properties—essential for an accurate modeling of the underlying population. A thorough population synthesis is beyond the scope of this paper. Here, we compare some of the observed properties of the 206 pulsars discovered by PALFA to those of the population that was known up until PALFA observations ceased in 2020 August. Consequently, we do not take into account recent discoveries by other surveys, for example those reported by the FAST Galactic Plane Pulsar Snapshot survey (GPPS; Han et al. 2021). To limit biases due to selection effects in our comparison, we exclude sources located in globular clusters and the Magellanic Clouds and only consider field pulsars within 10° of the Galactic plane that were discovered in nontargeted searches, resulting in a set of 1624 (non-PALFA) radio pulsars. Their properties were taken from the ATNF catalog (version 1.64). The same set of 1624 known sources is used throughout the analysis described below, except when the parameter being examined is not available for a given object, in which case the pulsar is excluded from the set.

³⁹ <https://heasarc.gsfc.nasa.gov/W3Browse/fermi/fermilpsc.html>

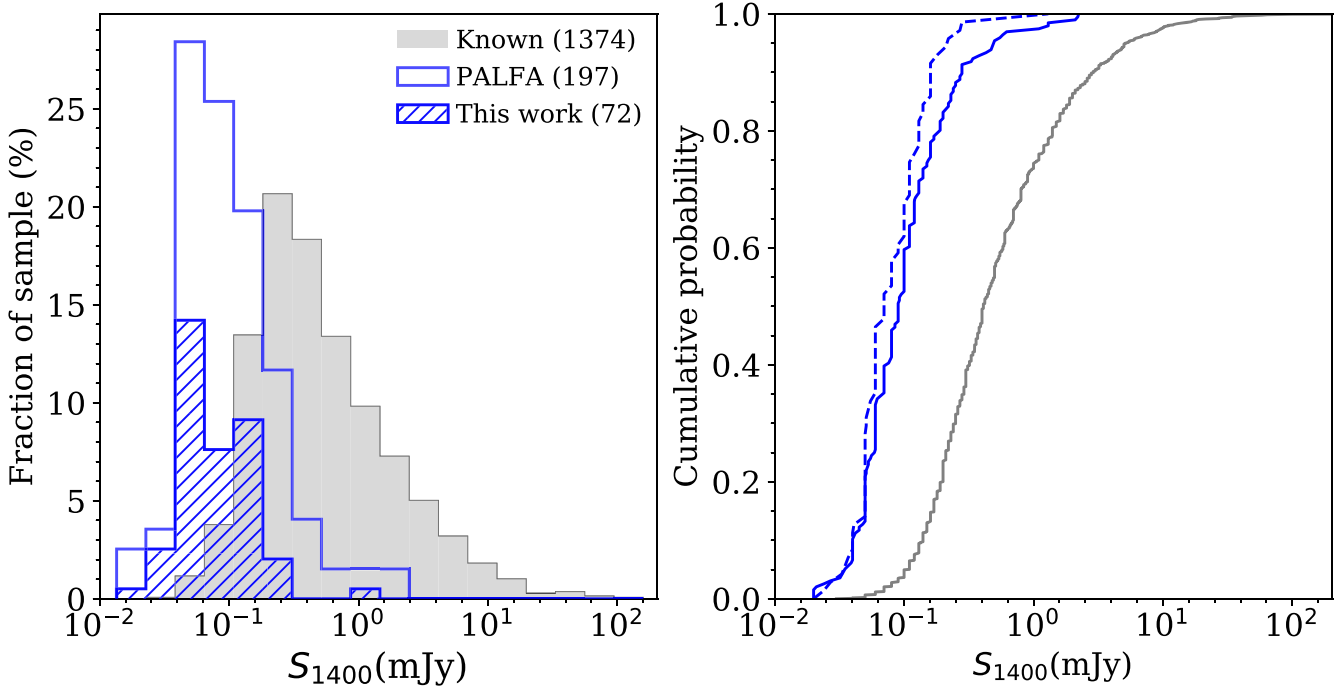


Figure 15. Probability density (left) and cumulative (right) distributions of average pulsed flux densities at 1400 MHz (S_{1400}) of field pulsars within $|b| < 10^\circ$ discovered in radio surveys other than PALFA (gray). PALFA sources are shown in blue, and the hatched pattern (left)/dashed line (right) corresponds to the pulsars featured in this work. Values of S_{1400} for non-PALFA objects were taken from the ATNF catalog (v. 1.64).

6.1. Flux Density

As a result of Arecibo’s large collecting area, the PALFA survey was able to detect pulsars to much lower flux densities than the average known population. In Figure 15, we compare the distribution of average pulsed flux densities S_{1400} of the PALFA sample to the known set. For pulsars presented in this work, we used the S_{1400} values presented in Tables 2 and 4. Sources with no reported S_{1400} in the ATNF catalog were excluded from the sample. The median S_{1400} value for PALFA discoveries is $100 \mu\text{Jy}$ ($70 \mu\text{Jy}$ for sources presented in this work), compared to $480 \mu\text{Jy}$ for the other known pulsars in the plane.

We are interested in the null hypothesis that the PALFA sample is statistically consistent with being the lower end of the brightness distribution of the known population in the plane. The null hypothesis is tested using a two-sided Anderson–Darling (AD) test. We chose the AD statistics over the commonly used Kolmogorov–Smirnov test as the former is more sensitive to deviations in the tails of distributions that depart from Gaussianity (Stephens 1974), which is where our interest lies. To extract accurate and stable statistics, empirical distribution functions for both the PALFA and known pulsar samples were generated through 10^3 iterations of bootstrap resampling. We find that the probability p of S_{1400} values for PALFA discoveries being drawn from the known population is < 0.001 . Combined with the distribution of average pulsed flux densities shown in Figure 15, we thus conclude that PALFA was successful in probing a fainter population.

6.2. Distance and Luminosity

We are now interested in determining whether the low flux density of PALFA discoveries is a result of the pulsars being located deep within the plane or if they are low-luminosity

objects. This essentially consists of examining the sample’s distribution in terms of distances, D , and inferred luminosity at 1400 MHz, L_{1400} , given the inverse-square law. We derive distances using both the NE2001 (D_{NE2001}) and YMW16 (D_{YMW16}) Galactic electron-density models, except for 97 pulsars for which precision distance measurements have been reported. For the remaining sources, luminosities ($L_{1400} = 4\pi S_{1400} D^2$) are calculated on a per-model basis. Pulsars with DM values exceeding the maximum Galactic contribution to the DM predicted along their respective lines of sight have poorly constrained distances, and are thus removed from their respective sample. That is the case for two PALFA-discovered pulsars whose DMs exceed the maximum Galactic DM predicted by the NE2001 model (PSR J1901+0459, $\text{DM} = 1108.0 \text{ pc cm}^{-3}$, Lazarus et al. 2015; PSR J2005+3547, $\text{DM} = 401.6 \text{ pc cm}^{-3}$, Nice et al. 2013). We note, however, that, in both cases, the amount of excess DM is small ($\sim 30 \text{ pc cm}^{-3}$) and within the typically assumed 25% uncertainty level for NE2001 predictions. As for the known pulsars sample, none have DMs larger than the maximum DM predicted by NE2001 but six do exceed the YMW16 predictions (PSR B1714–34, $\text{DM} = 587.7 \text{ pc cm}^{-3}$, Johnston et al. 1992; PSR J0837–24, $\text{DM} = 142.8 \text{ pc cm}^{-3}$, Burke-Spolaor et al. 2011; PSR J1305–6256, $\text{DM} = 967 \text{ pc cm}^{-3}$, Manchester et al. 2001; PSR J1321–5922, $\text{DM} = 383 \text{ pc cm}^{-3}$, Keith et al. 2009; PSR J1324–6146, $\text{DM} = 828 \text{ pc cm}^{-3}$ and PSR J1637–4335, $\text{DM} = 608 \text{ pc cm}^{-3}$, Kramer et al. 2003).

In Figure 16, we compare the distribution in distances and luminosities of PALFA discoveries against the known pulsars. PALFA-discovered objects have a median distance of 6.8 kpc (for both electron-density models), about 1.5 more distant than the median value of 4.6 kpc for the other radio pulsars in the plane. The pulsars featured in this work are even

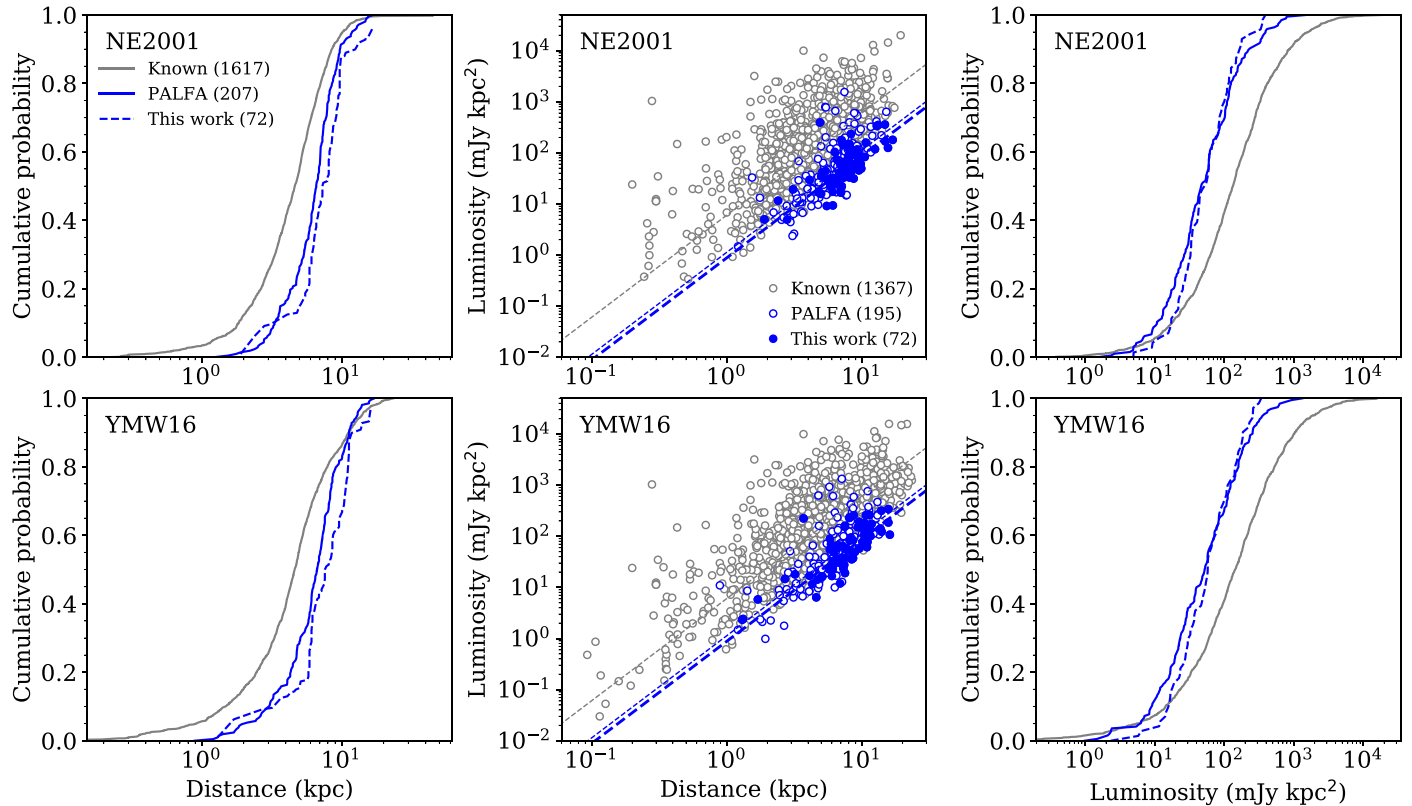


Figure 16. Distribution of DM-predicted distances and inferred luminosities at 1400 MHz of known pulsars within 10° of the Galactic plane discovered in nontargeted radio searches, computed for both the NE2001 (top) and YMW16 (bottom) models. Luminosities were estimated using DM distances and S_{1400} values, and should therefore be interpreted with caution. In blue are PALFA discoveries, and sources discovered by other surveys are shown in gray. Lines in the middle panels correspond to lines of constant flux densities, valued at the median S_{1400} for each sample (see text). Values of distances and luminosities for non-PALFA objects were computed from the DM, position and S_{1400} measurements reported in the ATNF catalog (see text).

more distant, with median distances of $D_{\text{NE2001}} = 7.3$ kpc and $D_{\text{YMW16}} = 7.6$ kpc.

We perform AD tests again with the bootstrap resampling method for the NE2001 and YMW16 models separately and find that, in both cases, the probability that the DM-derived distances of PALFA sources are drawn from the same distribution as the known sample is $p < 0.02$. Unsurprisingly, the AD test also rejects the null hypothesis for luminosities ($p < 0.01$). We therefore conclude that PALFA has indeed uncovered a distant population deep in the Galactic plane, but cannot independently evaluate the contribution of the intrinsic luminosity distributions to the observed flux densities. However, it is important to stress here that both parameters used in estimating luminosities have large uncertainties, and distances inferred from DMs can be incorrect by factors of 5 or more (e.g., Deller et al. 2019). The above results should therefore be interpreted with caution.

6.3. Propagation Effects

We now explore how propagation effects have impacted the observed population in the plane. To mitigate the effect of dispersion smearing, PALFA has observed the Galactic plane at 1400 MHz with high spectral (0.33 MHz) and temporal ($64 \mu\text{s}$) resolutions. Because the PALFA sample has very few sources showing significant scattering, we only investigate the effect of pulse dispersion. In terms of DM distribution, an AD test indicates that the DMs of PALFA sources are consistent with the known population ($p \sim 0.1$). However, this is not very informative since selection biases arising from propagation in

the ISM only become significant when pulse broadening becomes comparable to the intrinsic pulse width. The irreversible intrachannel smearing due to dispersion is detrimental to survey sensitivities, even more so for fast-spinning (i.e., highly recycled) pulsars because of their small pulse widths. Hence, examining the measured DMs versus P s of known pulsars provides insight into observational biases caused by the ISM affecting a survey.

In Figure 17, we show the distribution of the DM/ P ratios (where DM is in pc cm^{-3} and P is in ms) of PALFA and non-PALFA pulsars discovered in the Galactic plane. One clear distinction between the two sets (in the top panels) is the presence of a significant second mode at high DM/ P values in the PALFA sample, which are primarily MSPs and make up for $\sim 20\%$ of the entire survey yield, whereas MSPs found through blind radio surveys (excluding PALFA sources) represent 6% of the known pulsars in the plane.⁴⁰ Moreover, of the three known pulsars with $\log \text{DM}/P > 2$, two were discovered by PALFA (J1850+0244, Scholz et al. 2015; J1903+0327, Champion et al. 2008; Freire et al. 2011).

When MSPs are excluded (bottom panels), the AD test suggests that there is no difference in the DM/ P distributions of the PALFA and known samples ($p \gtrsim 0.25$), whereas when MSPs are included, the AD test probability drops to $p < 0.01$. Hence, the superior ability of PALFA to mitigate pulse dispersion and hence probe deep into high-electron-density

⁴⁰ Radio searches targeting the position of unidentified Fermi point sources have led to an increase in MSP discoveries this past decade (e.g., Ransom et al. 2011; Kerr et al. 2012; Camilo et al. 2015; Fonseca et al. 2021).

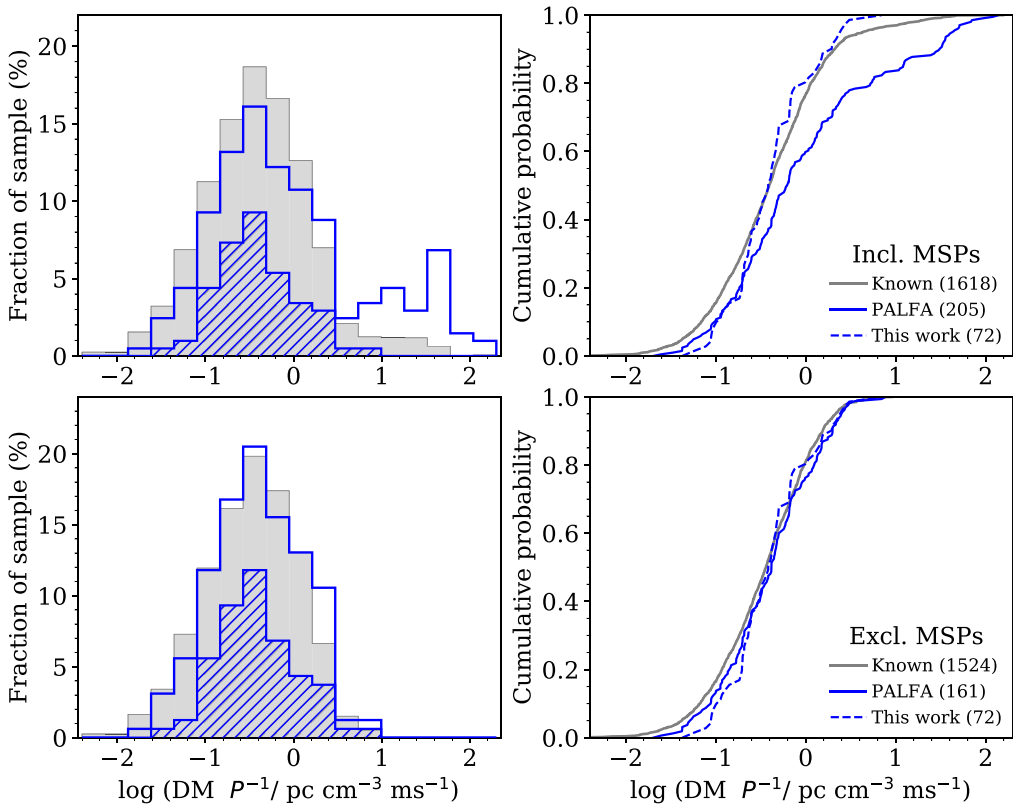


Figure 17. Distribution of DM/P ratios of pulsars, including (top) and excluding (bottom) MSPs, within $|b| < 10^\circ$ of the Galactic plane discovered in nontargeted radio searches. PALFA discoveries are shown in blue and in gray are sources found by surveys other than PALFA. The hatched regions/dashed lines in blue are pulsars presented in this work. RRATs with no available P measurements were excluded from both samples.

regions has only had a statistically significant impact in uncovering the highly dispersed MSP population within the plane.

7. Survey Status

On 2020 August 10, operations at Arecibo stopped when an auxiliary cable slipped out of its socket atop one of three towers supporting the platform, causing damage to the dish below. This was the first cable failure of a series that led to the collapse of the platform on 2020 December 1. PALFA therefore terminated⁴¹ before completion. Here, we provide an updated accounting of the survey sky coverage and completeness for potential use in future population synthesis work.

To optimize the use of telescope resources, PALFA observed commensally with the Zone of Avoidance (Henning et al. 2010) and the radio recombination lines (Liu et al. 2013) projects. Observations in the outer Galaxy were led by our commensal partners, while we led observations in the inner Galaxy. Our pointing strategy for the inner-Galaxy region prioritized $|b| < 3^\circ$ regions before moving on to higher Galactic latitudes. To maximize efficiency and sensitivity, our pointing grid sampled the sky by interleaving three ALFA pointings such that the gain at any sky position was equal to or greater than the receiver half-maximum gain (see Cordes et al. 2006). Rather than maximizing the sky coverage, our commensal partners adopted a strategy where certain longitude/latitude ranges are densely sampled; most pointings in the outer-Galaxy region were reobserved several times. While that approach is

not optimal for deep pulsar surveying in terms of survey speed, searching those data sets has benefits for the detection of erratic sources. For instance, one of our FRBs and four RRATs were detected only once in outer Galaxy pointings that were observed three times or more.

From 2004 to 2009, PALFA observations were recorded with the Wide-Band Arecibo Pulsar Processor (WAPP) spectrometers (Dowd et al. 2000), which processed 100 MHz passbands centered at 1.42 GHz for each of the seven ALFA beams. We found a total of 56 pulsars and covered 200 sq. deg. of the sky with WAPP: 110 sq. deg. in the inner-Galaxy region (38 normal pulsars, 10 MSPs and four RRATs), and 90 sq. deg. in the outer region (three normal pulsars and one RRAT). More details on the WAPP data collection volumes can be found in Allen et al. (2013).

In mid-2009, we switched to using the Mock spectrometers, which provided an observing bandwidth three times wider than that of the WAPP system (see Section 2.1 for more details on the Mock instrument parameters). The increased bandwidth, multibit depth and polyphase filterbank design of the Mock spectrometers improved the survey sensitivity and increased its robustness to RFI. In fact, our discovery rate was nearly doubled even though there was some overlap in the WAPP and Mock sky coverage. With Mock, we discovered a total of 151 pulsars and three FRBs: 147 pulsars (including 35 MSPs and 11 RRATs) and one FRB in the inner region, and four pulsars (including one MSP and two RRATs) and two FRBs in the outer region, after covering 218 and 114 sq. deg. in the inner and outer regions, respectively.

Approximately 16% of the WAPP pointings were reobserved with Mock during the first year of transition, and it was

⁴¹ PALFA observations were last conducted on 2020 August 9, a few hours prior to the first cable break.

Table 9
Census of PALFA Survey Data

No. Beams	No. Unique Sky Positions	Sky Coverage (sq. deg.)	Completeness, $ b < 2^\circ$ (%)	Completeness, $ b < 3^\circ$ (%)	Completeness, $ b < 5^\circ$ (%)
Inner Galaxy	86705	84846	218	95	89
Outer Galaxy	123234	44465	114	37	30

Note. Only Mock beams that were successfully processed and analyzed are listed. Likewise, the WAPP data sets are excluded from the sky coverage and completeness values. We note that each ALFA pointing consists of seven beams that are processed independently. As such, the values provided here represent the number of searched beams rather than pointings. That provides an accurate accounting by excluding failed beam(s) from a pointing. The difference in the number of beams versus unique sky positions are due to reobservations of a pointing, which is especially significant for outer-Galaxy data sets.

our intention to eventually reobserve all remaining WAPP pointings so that the sensitivity of the survey would be uniform across the PALFA sky. A breakdown of the Mock survey data, sky coverage and completeness for both the inner and outer regions is provided in Table 9. Values presented in the table only include data sets that have been processed and inspected, which represents approximately 96% of the total number of beams collected with Mock. The remaining 4% could not be searched, largely due to severe RFI contamination which rendered the data unusable.

Figure 18 shows the sky locations of the beams that were searched, collected with either Mock (blue) or WAPP (green), as well as the positions of failed beams (red). It also shows the positions of our pulsar (orange) and FRB (yellow) discoveries. We provide lists of all the processed beams and relevant information as Supporting Information with the online version of the paper. Further details regarding processing of WAPP and Mock data can be found in Cordes et al. (2006) and Lazarus et al. (2015), respectively. Information relating to detections of known sources, which we do not discuss here, will be reported in a future publication.

8. Conclusions

In this work, we have presented the results of long-term monitoring on 72 pulsars found by the PALFA survey, plus estimates of their emission properties: DMs, scattering times, and flux densities. All of these quantities are important for characterizing the population. Pulsar timing is especially important since it allows estimates of fundamental properties of the NS like the dipolar magnetic field strength, characteristic age, spin-down power, glitching behavior and possible membership of binary systems.

Overall, the pulsars characterized here have much lower flux densities than the previously known population in the survey area, a demonstration of the sensitivity of the PALFA survey and also, in part, a consequence of the fact that these pulsars were not discovered by previous surveys that covered the search region. Furthermore, the pulsar sample in this work is also faint compared to the previously published PALFA slow pulsars: those were either found and timed earlier with the less-sensitive WAPP spectrometers (Nice et al. 2013), or were later timed at Jodrell Bank, which can only follow up the brighter systems (Lyne et al. 2017a, 2017b). Thus, the pulsars presented in this work tend to be among the faintest PALFA discoveries, which are already quite faint in comparison to the known population.

These faint pulsars could, *a priori*, either be low-luminosity pulsars relatively nearby, or very luminous pulsars at very large distances. We find that the PALFA discoveries—and even more the group studied in this work—represent a low-

luminosity population in comparison to the population previously discovered in the survey region. From their positions in the $P - \dot{P}$ diagram, we additionally conclude that they represent an older, less energetic population than that previously known in the survey region. This is not a selection effect against the discovery of young, fast-spinning pulsars: the PALFA survey has found many more MSPs than previous surveys in the survey area. In fact, because of RFI, the PALFA survey is biased against the detection of very slow pulsars (Lazarus et al. 2015). Without RFI, we probably would have found an even slower, older and less energetic population. Thus, the most luminous pulsars in the survey region were already discovered in previous, less-sensitive surveys. A possible interpretation is that, for the population of luminous pulsars, those surveys were already covering the full useful volume of our Galaxy, i.e., the extra survey volume provided by the PALFA survey for this type of pulsar is likely beyond our Galaxy. Another consequence of this is that, for the population of highly luminous pulsars, the average distance has remained the same, since few new ones have been found. It is for the less luminous pulsar population that the extra survey volume provided by the PALFA survey is still within the Galaxy. Since those are being discovered at larger distances than was possible before, this results in significant increases in the average distances: this is 7–8 kpc for all new PALFA slow pulsars, significantly larger than the average 4.6 kpc for the previously known pulsars in the survey region.

Among the sources presented in this work are a wide variety of glitching, mode-changing, intermittent and nulling pulsars; we characterize the occurrence of these phenomena within our pulsar sample in some detail. Intermittent, mode-changing and nulling pulsars are especially common among the slow, older and fainter pulsar population being found by our survey (Nice et al. 2013; Lyne et al. 2017a, 2017b). In particular, the four new intermittent pulsars found by PALFA—J1855+0626 and J1952+2513 presented here, plus J1910+0517 and J1929+1357, described by Lyne et al. (2017a)—more than double the population of intermittent pulsars known before this survey. More detailed studies of these objects may help to improve our understanding of the physics of pulsar magnetospheres. The statistics of RRATs, nulling and intermittent pulsars are also fundamental for better estimates of the true size of the NS population in the Galaxy. Our results indicate that there are many more such objects in the Galaxy than have been detected thus far.

Also among our discoveries is a new binary pulsar, PSR J1954+2529, with a wide ($P_b = 82.7$ days) and eccentric ($e = 0.114$) orbit. This is a member of a relatively rare population of binary pulsars which appear to have not been recycled, and is similar to PSR J1932+1500, which was also

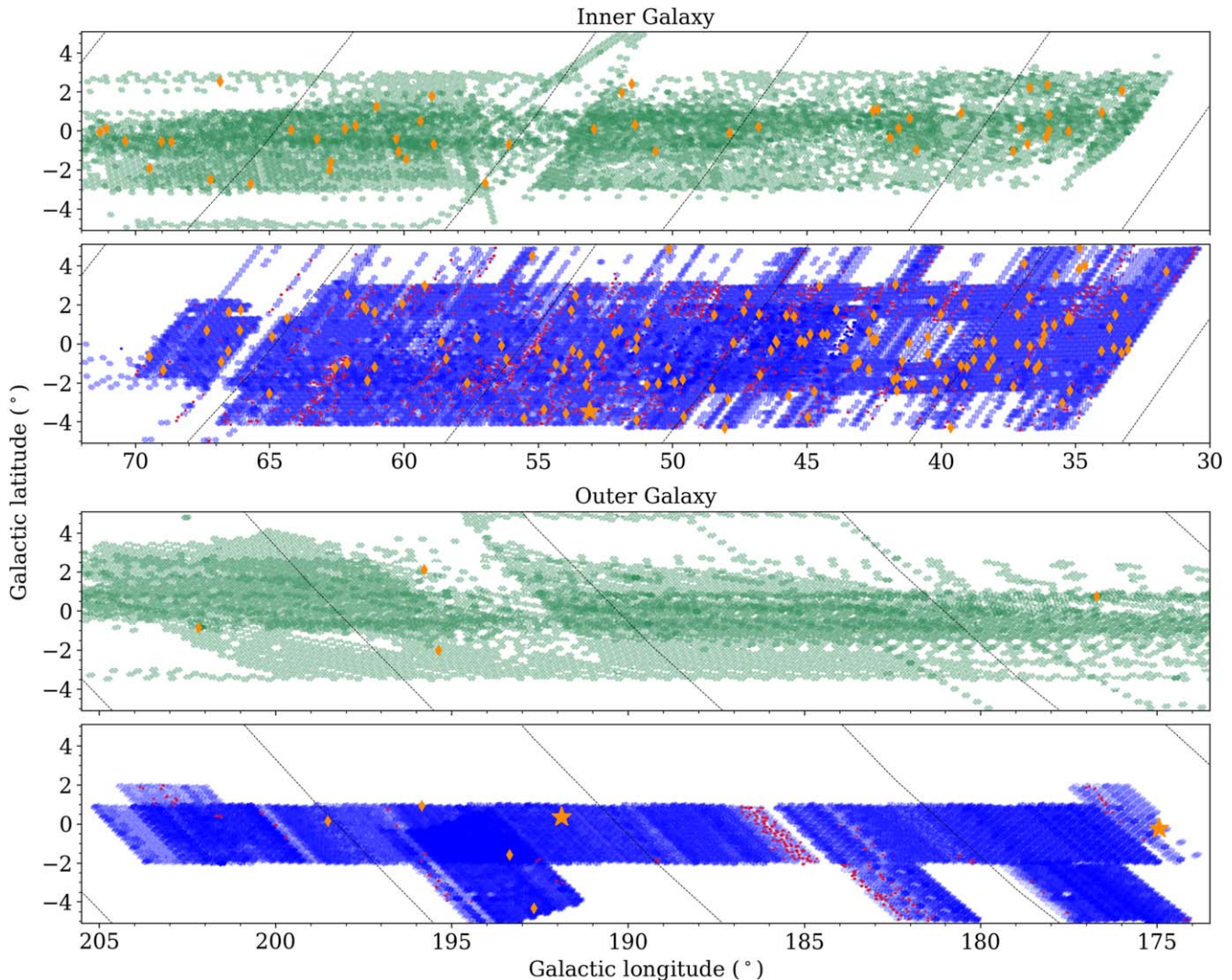


Figure 18. Sky map showing the sky position of analyzed PALFA beams. Beams recorded with the WAPP (first and third panels) and Mock (second and fourth panels) spectrometers are shown in green and blue, respectively, and red points correspond to beams for which processing failed due to high levels of RFI. Observing density at each sky position scales with the marker opacity. All pulsars discovered by the survey are shown as orange diamonds, while the three orange stars are FRB discoveries. Dashed black lines are lines of constant decl..

(The data used to create this figure are available.)

discovered by the PALFA survey (Lyne et al. 2017b). The origin of these systems, which we discuss in detail in this work, is still uncertain: some of them could be progenitors to LMXBs, while others could result from weakly interacting PSR—MS star systems. Understanding this is important: given the small characteristic ages of the pulsars in these systems (of the order of Myr, compared to Gyr for MSPs), it is clear that they form at comparable or even larger rates than the better-known MSP binaries.

In this work we also describe the PALFA survey status, and summarize the final sky coverage. The pulsars described in this work represent approximately one-third of PALFA’s discoveries to date: 142 normal pulsars, 46 MSPs, 19 RRATs and three FRBs. All data collected after 2015 have been searched with an upgraded full-resolution pipeline (Parent et al. 2018; Patel et al. 2018); reprocessing of Mock data collected prior to 2015 is ongoing, as is the Einstein@Home search of the later part of the survey data. Timing observations are being conducted with CHIME/Pulsar and Lovell on \sim 15 MSPs

(Parent et al., in prep., Haniewicz et al., in prep.), eight normal pulsars and 15 RRATs (Doskoch et al., in prep.) that were last discovered by PALFA (see Table 2) and for which timing solutions have not yet been determined. Thus, although the PALFA survey was cut short by the demise of the Arecibo 305 m telescope, we expect to report many further discoveries.

The Arecibo observatory is operated by the University of Central Florida, Ana G. Mendez-Universidad Metropolitana, and Yang Enterprises under a cooperative agreement with the National Science Foundation (NSF; AST-1744119). Pulsar research at Jodrell Bank and access to the Lovell Telescope is supported by a Consolidated Grant from the UKs Science and Technology Facilities Council. The National Radio Astronomy Observatory is a facility of the National Science Foundation operated under cooperative agreement by Associated Universities, Inc. We are grateful to the staff of the Dominion Radio Astrophysical Observatory, which is operated by the National Research Council of Canada. CHIME is funded by a grant from the Canada Foundation for Innovation (CFI) 2012 Leading

Edge Fund (Project 31170) and by contributions from the provinces of British Columbia, Québec and Ontario. The CHIME/FRB Project, which enabled development in common with the CHIME/Pulsar instrument, is funded by a grant from the CFI 2015 Innovation Fund (Project 33213) and by contributions from the provinces of British Columbia and Québec, and by the Dunlap Institute for Astronomy and Astrophysics at the University of Toronto.

Additional support was provided by the Canadian Institute for Advanced Research (CIFAR), McGill University and the McGill Space Institute thanks to the Trottier Family Foundation, and the University of British Columbia. The CHIME/Pulsar instrument hardware was funded by NSERC RTI-1 grant No. EQPEQ 458893-2014. This research was enabled in part by support provided by WestGrid, Compute Canada and Calcul Québec. Work at the Naval Research Laboratory was supported by the NASA Fermi program. This work was supported by the Max Planck Gesellschaft and by NSF grant Nos. 0555655, 1104617, 1104902, 1105572 and 1816904.

We thank all Einstein@Home volunteers, especially those whose computers found pulsars with the highest statistical significance. PSR J1851+0241: Mel S. Stark, Somonauk, Illinois, USA and “TRON”. PSR J1853+0029: “[TiDC] Chulma—S’nergy” and Rodolfo Manalac, Queens College, CUNY, Flushing, New York, USA. PSR J1855+0306: Jeroen Moetwil, Flagstaff, Arizona, USA and Robert E. Inman Jr., Virginia Beach, Virginia, USA. PSR J1859+0345: James S. Drews, UW-Madison, Wisconsin, USA and “juergenstoetzel”. PSR J1909+1205: Alexandr Jungwirth, Prague, Czech Republic and “Administrator”. PSR J1910+0710: John Murphy, Austin, Texas, USA and “Grey”. PSR J1910+1017: “mglogan” and Dave and Emma Johnston, Jacksonville, Florida, USA. PSR J1911+0925: Matthias Pfister, Gland, Switzerland and Ryan D. Morton, Ann Arbor, Michigan, USA. PSR J1914+1428: John-Luke Peck, Bellevue, Washington, USA and Mark Henderson, Russellville, Tennessee, USA. PSR J1948+2819: “Chuck Claybaugh” and “Orange_Crunch”. PSR J1952+2513: “Joe” and Jarmo Kahila, Vantaa, Finland. PSR J1953+2819: “Rojer” and “testkermit”. PSR J1955+2930: “Przemek Wisialski” and Gary S. Grant II, Nelsonville, Ohio, USA.

We thank the anonymous referee for their careful reading of the manuscript and helpful suggestions. We also thank Thomas Tauris for a useful comments on the evolution of PSR J1954+2529, and Rosie Chen for the discussion on the infrared nondetection of its companion. We also thank the FAST GPPS survey collaboration for noticing that we were reporting harmonic frequencies for two pulsars in the initial version of this manuscript.

E.P. is a Vanier Canada Graduate Scholar. M.A.M., F.C., A.B., S.C., J.M.C., E.F., B.W.M., S.M.R., and I.H.S. are members of the NANOGrav Physics Frontiers Center, which is supported by the NSF award PHY 1430284. S.C. and J.M.C. acknowledge support from the National Science Foundation (AAG 1815242). F.A.D. is supported by the University of British Columbia Four Year Doctoral Fellowship. V.M.K> holds the Lorne Trottier Chair in Astrophysics & Cosmology and a Distinguished James McGill Professorship and receives support from an NSERC Discovery Grant and Herzberg Award, from an R. Howard Webster Foundation Fellowship from the Canadian Institute for Advanced Research (CIFAR), and from the FRQNT Centre de Recherche en Astrophysique du Québec. J.W.M. is a CITA Postdoctoral Fellow and is

supported by the Natural Sciences and Engineering Research Council of Canada (CITA 490888-16). S.M.R. is a CIFAR Fellow.

Software: PRESTO (Ransom 2011) available at <https://github.com/scottransom/presto>, PSRCHIVE (Hotan et al. 2004) available at <http://psrchive.sourceforge.net/index.shtml>, TEMPO (Nice et al. 2015), ASCL: <https://ascl.net/1509.002>.

ORCID iDs

- E. Parent <https://orcid.org/0000-0002-0430-6504>
- P. C. C. Freire <https://orcid.org/0000-0003-1307-9435>
- B. B. P. Perera <https://orcid.org/0000-0002-8509-5947>
- M. A. McLaughlin <https://orcid.org/0000-0001-7697-7422>
- B. Allen <https://orcid.org/0000-0003-4285-6256>
- A. Brazier <https://orcid.org/0000-0001-6341-7178>
- F. Camilo <https://orcid.org/0000-0002-1873-3718>
- S. Chatterjee <https://orcid.org/0000-0002-2878-1502>
- J. M. Cordes <https://orcid.org/0000-0002-4049-1882>
- F. Crawford <https://orcid.org/0000-0002-2578-0360>
- J. S. Deneva <https://orcid.org/0000-0003-1226-0793>
- F. A. Dong <https://orcid.org/0000-0003-4098-5222>
- R. D. Ferdman <https://orcid.org/0000-0002-2223-1235>
- E. Fonseca <https://orcid.org/0000-0001-8384-5049>
- J. W. T. Hessels <https://orcid.org/0000-0003-2317-1446>
- V. M. Kaspi <https://orcid.org/0000-0001-9345-0307>
- B. Knispel <https://orcid.org/0000-0003-3168-0929>
- J. van Leeuwen <https://orcid.org/0000-0001-8503-6958>
- R. S. Lynch <https://orcid.org/0000-0001-5229-7430>
- B. M. Meyers <https://orcid.org/0000-0001-8845-1225>
- J. W. McKee <https://orcid.org/0000-0002-2885-8485>
- M. B. Mickaliger <https://orcid.org/0000-0001-6798-5682>
- C. Patel <https://orcid.org/0000-0003-3367-1073>
- S. M. Ransom <https://orcid.org/0000-0001-5799-9714>
- P. Scholz <https://orcid.org/0000-0002-7374-7119>
- I. H. Stairs <https://orcid.org/0000-0001-9784-8670>
- B. W. Stappers <https://orcid.org/0000-0001-9242-7041>
- C. M. Tan <https://orcid.org/0000-0001-7509-0117>
- W. W. Zhu <https://orcid.org/0000-0001-5105-4058>

References

- Abdo, A. A., Ajello, M., Allafort, A., et al. 2013, *ApJS*, **208**, 17
- Abdollahi, S., Acero, F., Ackermann, M., et al. 2020, *ApJS*, **247**, 33
- Abt, H. A. 1983, *ARA&A*, **21**, 343
- Allafort, A., Baldini, L., Ballet, J., et al. 2013, *ApJL*, **777**, L2
- Allen, B., Knispel, B., Cordes, J. M., et al. 2013, *ApJ*, **773**, 91
- Anderson, L. D., Wang, Y., Bihl, S., et al. 2017, *A&A*, **605**, A58
- Anderson, P. W., & Itoh, N. 1975, *Natur*, **256**, 25
- Antoniadis, J., Bassa, C. G., Wex, N., Kramer, M., & Napiwotzki, R. 2011, *MNRAS*, **412**, 580
- Antoniadis, J., Freire, P. C. C., Wex, N., et al. 2013, *Sci*, **340**, 448
- Archibald, A. M., Gusinskaia, N. V., Hessels, J. W. T., et al. 2018, *Natur*, **559**, 73
- Arons, J. 1996, *SSRv*, **75**, 235
- Arzoumanian, Z., Baker, P. T., Brazier, A., et al. 2018, *ApJ*, **859**, 47
- Backer, D. C. 1970a, *Natur*, **228**, 1297
- Backer, D. C. 1970b, *Natur*, **228**, 42
- Bartel, N., Morris, D., Sieber, W., & Hankins, T. H. 1982, *ApJ*, **258**, 776
- Bassa, C. G., Brisken, W. F., Nelemans, G., et al. 2011, *MNRAS*, **412**, L63
- Bell, J. F., Bessell, M. S., Stappers, B. W., Bailes, M., & Kaspi, V. M. 1995, *ApJL*, **447**, L117
- Bhat, N. D. R., Bailes, M., & Verbiest, J. P. W. 2008, *PhRvD*, **77**, 124017
- Bhattacharyya, B., Lyne, A. G., Stappers, B. W., et al. 2018, *MNRAS*, **477**, 4090
- Burgay, M., Stappers, B., Bailes, M., et al. 2019, *MNRAS*, **484**, 5791
- Burke-Spolaor, S., Bailes, M., Johnston, S., et al. 2011, *MNRAS*, **416**, 2465
- Camilo, F., Kerr, M., Ray, P. S., et al. 2015, *ApJ*, **810**, 85

- Camilo, F., Ransom, S. M., Chatterjee, S., Johnston, S., & Demorest, P. 2012, *ApJ*, **746**, 63
- Cerutti, B., & Beloborodov, A. M. 2017, *SSRv*, **207**, 111
- Champion, D. J., Ransom, S. M., Lazarus, P., et al. 2008, *Sci*, **320**, 1309
- CHIME/Pulsar Collaboration, Amiri, M., Bandura, K. M., et al. 2021, *ApJS*, **255**, 5
- Cordes, J. M., Freire, P. C. C., Lorimer, D. R., et al. 2006, *ApJ*, **637**, 446
- Cordes, J. M., & Lazio, T. J. W. 2001, *ApJ*, **549**, 997
- Cordes, J. M., & Lazio, T. J. W. 2002, arXiv:[astro-ph/0207156](#)
- Crawford, F., Stovall, K., Lyne, A. G., et al. 2012, *ApJ*, **757**, 90
- Cronyn, W. M. 1970, *Sci*, **168**, 1453
- D'Antona, F., & Tailo, M. 2020, arXiv:[2011.11385](#)
- Deller, A. T., Goss, W. M., Brisken, W. F., et al. 2019, *ApJ*, **875**, 100
- Deneva, J. S., Cordes, J. M., McLaughlin, M. A., et al. 2009, *ApJ*, **703**, 2259
- Deneva, J. S., Freire, P. C. C., Cordes, J. M., et al. 2012, *ApJ*, **757**, 89
- Dewey, R. J., Taylor, J. H., Weisberg, J. M., & Stokes, G. H. 1985, *ApJL*, **294**, L25
- Dowd, A., Sisk, W., & Hagen, J. 2000, in ASP Conf. Ser. 202, IAU Colloq. 177: Pulsar Astronomy—2000 and Beyond, ed. M. Kramer, N. Wex, & R. Wielebinski (San Francisco, CA: ASP), **275**
- Driesssen, L. N., Domček, V., Vink, J., et al. 2018, *ApJ*, **860**, 133
- Duchêne, G., Simon, T., Eisloffel, J., & Bouvier, J. 2001, *A&A*, **379**, 147
- DuPlain, R., Ransom, S., Demorest, P., et al. 2008, *Proc. SPIE*, **7019**, 70191D
- Esamdin, A., Lyne, A. G., Graham-Smith, F., et al. 2005, *MNRAS*, **356**, 59
- Espinosa, C. M., Lyne, A. G., Stappers, B. W., & Kramer, M. 2011, *MNRAS*, **414**, 1679
- Faucher-Giguère, C.-A., & Kaspi, V. M. 2006, *ApJ*, **643**, 332
- Ferdman, R. D., Freire, P. C. C., Perera, B. B. P., et al. 2020, *Natur*, **583**, 211
- Ferdman, R. D., Stairs, I. H., Kramer, M., et al. 2013, *ApJ*, **767**, 85
- Filippenko, A. V., & Radhakrishnan, V. 1982, *ApJ*, **263**, 828
- Fonseca, E., Cromartie, H. T., Pennucci, T. T., et al. 2021, *ApJL*, **915**, L12
- Freire, P. C. C., Bassa, C. G., Wex, N., et al. 2011, *MNRAS*, **412**, 2763
- Gajjar, V., Joshi, B. C., & Kramer, M. 2012, *MNRAS*, **424**, 1197
- Green, D. A. 2019, *JApA*, **40**, 36
- Gürgencioğlu, E., Ge, M. Y., Yuan, J. P., & Zhou, S. Q. 2020, arXiv:[2011.14788](#)
- Gwinn, C. R., Johnson, M. D., Smirnova, T. V., & Stinebring, D. R. 2011, *ApJ*, **733**, 52
- Han, J. L. 2017, *ARA&A*, **55**, 111
- Han, J. L., Wang, C., Wang, P. F., et al. 2021, *RAA*, **21**, 107
- Henning, P. A., Springob, C. M., Minchin, R. F., et al. 2010, *AJ*, **139**, 2130
- Ho, W. C. G., Ng, C. Y., Lyne, A. G., et al. 2017, *MNRAS*, **464**, 1211
- Hobbs, G., Lyne, A. G., Kramer, M., Martin, C. E., & Jordan, C. 2004, *MNRAS*, **353**, 1311
- Hotan, A. W., van Straten, W., & Manchester, R. N. 2004, *PASA*, **21**, 302
- Hulse, R. A., & Taylor, J. H. 1975, *ApJL*, **195**, L51
- Janssen, G. H., & Stappers, B. W. 2006, *A&A*, **457**, 611
- Johnson, M. D., & Gwinn, C. R. 2012, *ApJ*, **755**, 179
- Johnston, S., Lyne, A. G., Manchester, R. N., et al. 1992, *MNRAS*, **255**, 401
- Johnston, S., Manchester, R. N., Lyne, A. G., Nicastro, L., & Spyromilio, J. 1994, *MNRAS*, **268**, 430
- Kalapotharakos, C., Harding, A. K., Kazanas, D., & Brambilla, G. 2017, *ApJ*, **842**, 80
- Kaspi, V. M., Bailes, M., Manchester, R. N., Stappers, B. W., & Bell, J. F. 1996, *Natur*, **381**, 584
- Kaspi, V. M., Lyne, A. G., Manchester, R. N., et al. 2000, *ApJ*, **543**, 321
- Keane, E. F., Kramer, M., Lyne, A. G., Stappers, B. W., & McLaughlin, M. A. 2011, *MNRAS*, **415**, 3065
- Keane, E. F., Ludovici, D. A., Eatough, R. P., et al. 2010, *MNRAS*, **401**, 1057
- Keith, M. J., Eatough, R. P., Lyne, A. G., et al. 2009, *MNRAS*, **395**, 837
- Kerr, M., Camilo, F., Johnson, T. J., et al. 2012, *ApJL*, **748**, L2
- Knispel, B., Lazarus, P., Allen, B., et al. 2011, *ApJL*, **732**, L1
- Knispel, B., Lyne, A. G., Stappers, B. W., et al. 2015, *ApJ*, **806**, 140
- Kramer, M., Bell, J. F., Manchester, R. N., et al. 2003, *MNRAS*, **342**, 1299
- Kramer, M., Lyne, A. G., O'Brien, J. T., Jordan, C. A., & Lorimer, D. R. 2006, *Sci*, **312**, 549
- Krishnakumar, M. A., Mitra, D., Naidu, A., Joshi, B. C., & Manoharan, P. K. 2015, *ApJ*, **804**, 23
- Kruckow, M. U., Tauris, T. M., Langer, N., Kramer, M., & Izzard, R. G. 2018, *MNRAS*, **481**, 1908
- Kulkarni, S. R. 1989, *AJ*, **98**, 1112
- Lazarus, P., Brazier, A., Hessels, J. W. T., et al. 2015, *ApJ*, **812**, 81
- Lazarus, P., Freire, P. C. C., Allen, B., et al. 2016, *ApJ*, **831**, 150
- Lee, L. C., & Jokipii, J. R. 1976, *ApJ*, **206**, 735
- Liu, B., McIntyre, T., Terzian, Y., et al. 2013, *AJ*, **146**, 80
- Lorimer, D. R., Camilo, F., & McLaughlin, M. A. 2013, *MNRAS*, **434**, 347
- Lorimer, D. R., Faulkner, A. J., Lyne, A. G., et al. 2006a, *MNRAS*, **372**, 777
- Lorimer, D. R., Lyne, A. G., McLaughlin, M. A., et al. 2012, *ApJ*, **758**, 141
- Lorimer, D. R., Nicastro, L., Lyne, A. G., et al. 1995, *ApJ*, **439**, 933
- Lorimer, D. R., Stairs, I. H., Freire, P. C., et al. 2006b, *ApJ*, **640**, 428
- Lyne, A., Hobbs, G., Kramer, M., Stairs, I., & Stappers, B. 2010, *Sci*, **329**, 408
- Lyne, A. G., Burgay, M., Kramer, M., et al. 2004, *Sci*, **303**, 1153
- Lyne, A. G., & McKenna, J. 1989, *Natur*, **340**, 367
- Lyne, A. G., Shemar, S. L., & Smith, F. G. 2000, *MNRAS*, **315**, 534
- Lyne, A. G., Stappers, B. W., Bogdanov, S., et al. 2017b, *ApJ*, **834**, 137
- Lyne, A. G., Stappers, B. W., Freire, P. C. C., et al. 2017a, *ApJ*, **834**, 72
- Lyne, A. G., Stappers, B. W., Keith, M. J., et al. 2015, *MNRAS*, **451**, 581
- Madsen, E. C., Stairs, I. H., Kramer, M., et al. 2012, *MNRAS*, **425**, 2378
- Manchester, R. N., Hobbs, G. B., Teoh, A., & Hobbs, M. 2005, *AJ*, **129**, 1993
- Manchester, R. N., Lyne, A. G., Camilo, F., et al. 2001, *MNRAS*, **328**, 17
- Manchester, R. N., & Taylor, J. H. 1977, Pulsars (San Francisco: Freeman)
- Martinez, J. G., Stovall, K., Freire, P. C. C., et al. 2015, *ApJ*, **812**, 143
- McKee, J. W., Janssen, G. H., Stappers, B. W., et al. 2016, *MNRAS*, **461**, 2809
- McKenna, J., & Lyne, A. G. 1990, *Natur*, **343**, 349
- McLaughlin, M. A., Lyne, A. G., Lorimer, D. R., et al. 2006, *Natur*, **439**, 817
- Ng, C., Kruckow, M. U., Tauris, T. M., et al. 2018, *MNRAS*, **476**, 4315
- Ng, C., Wu, B., Ma, M., et al. 2020, *ApJ*, **903**, 81
- Nice, D., Demorest, P., Stairs, I., et al. 2015, Tempo: Pulsar timing data analysis, Astrophysics Source Code Library, ascl:[1509.002](#)
- Nice, D. J., Altieri, E., Bogdanov, S., et al. 2013, *ApJ*, **772**, 50
- Olausen, S. A., & Kaspi, V. M. 2014, *ApJS*, **212**, 6
- Parent, E., Kaspi, V. M., Ransom, S. M., et al. 2018, *ApJ*, **861**, 44
- Parent, E., Kaspi, V. M., Ransom, S. M., et al. 2019, *ApJ*, **886**, 148
- Patel, C., Agarwal, D., Bhardwaj, M., et al. 2018, *ApJ*, **869**, 181
- Pletsch, H. J., Guillermot, L., Allen, B., et al. 2012, *ApJL*, **755**, L20
- Pol, N., McLaughlin, M., Lorimer, D. R., & Garver-Daniels, N. 2021, *ApJ*, **912**, 22
- Rankin, J. M. 1993, *ApJ*, **405**, 285
- Ransom, S. 2011, PRESTO: Pulsar Exploration and Search Toolkit, Astrophysics Source Code Library, ascl:[1107.017](#)
- Ransom, S. M., Ray, P. S., Camilo, F., et al. 2011, *ApJL*, **727**, L16
- Ray, P. S., Abdo, A. A., Parent, D., et al. 2012, arXiv:[1205.3089](#)
- Ray, P. S., Kerr, M., Parent, D., et al. 2011, *ApJS*, **194**, 17
- Redman, S. L., Wright, G. A. E., & Rankin, J. M. 2005, *MNRAS*, **357**, 859
- Remazeilles, M., Dickinson, C., Banday, A. J., Bigot-Sazy, M. A., & Ghosh, T. 2015, *MNRAS*, **451**, 4311
- Rickett, B., Johnston, S., Tomlinson, T., & Reynolds, J. 2009, *MNRAS*, **395**, 1391
- Rickett, B. J. 1977, *ARA&A*, **15**, 479
- Ruderman, M., Zhu, T., & Chen, K. 1998, *ApJ*, **492**, 267
- Sana, H., & Evans, C. J. 2011, in IAU Symp. 272, Active OB Stars: Structure, Evolution, Mass Loss, and Critical Limits, ed. C. Neiner et al. (Cambridge: Cambridge Univ. Press), **474**
- Schlafly, E. F., & Finkbeiner, D. P. 2011, *ApJ*, **737**, 103
- Scholz, P., Kaspi, V. M., Lyne, A. G., et al. 2015, *ApJ*, **800**, 123
- Scholz, P., Spitler, L. G., Hessels, J. W. T., et al. 2016, *ApJ*, **833**, 177
- Shannon, R. M., Johnston, S., & Manchester, R. N. 2014, *MNRAS*, **437**, 3255
- Skrutskie, M. F., Cutri, R. M., Stiening, R., et al. 2006, *AJ*, **131**, 1163
- Smith, D. A., Bruel, P., Cognard, I., et al. 2019, *ApJ*, **871**, 78
- Spitler, L. G., Cordes, J. M., Hessels, J. W. T., et al. 2014, *ApJ*, **790**, 101
- Spitler, L. G., Scholz, P., Hessels, J. W. T., et al. 2016, *Natur*, **531**, 202
- Stairs, I. H., Lyne, A. G., Kramer, M., et al. 2019, *MNRAS*, **485**, 3230
- Stairs, I. H., Lyne, A. G., & Shemar, S. L. 2000, *Natur*, **406**, 484
- Stephens, M. A. 1974, *J. Am. Stat. Assoc.*, **69**, 730
- Stinebring, D. R., McLaughlin, M. A., Cordes, J. M., et al. 2001, *ApJL*, **549**, L97
- Stovall, K. 2013, PhD Thesis, The Univ. of Texas at San Antonio
- Stovall, K., Allen, B., Bogdanov, S., et al. 2016, *ApJ*, **833**, 192
- Stovall, K., Freire, P. C. C., Chatterjee, S., et al. 2018, *ApJL*, **854**, L22
- Swiggum, J. K., Lorimer, D. R., McLaughlin, M. A., et al. 2014, *ApJ*, **787**, 137
- Tauris, T. M., Kramer, M., Freire, P. C. C., et al. 2017, *ApJ*, **846**, 170
- Tauris, T. M., Langer, N., & Kramer, M. 2012, *MNRAS*, **425**, 1601
- Tauris, T. M., & Savonije, G. J. 1999, *A&A*, **350**, 928
- Tauris, T. M., & Sennels, T. 2000, *A&A*, **355**, 236
- Taylor, J. H. 1992, *RSPTA*, **341**, 117
- Thorsett, S. E., Arzoumanian, Z., McKinnon, M. M., & Taylor, J. H. 1993, *ApJL*, **405**, L29

- Tuntsov, A. V., Bignall, H. E., & Walker, M. A. 2013, *MNRAS*, **429**, 2562
van Kerkwijk, M. H., & Kulkarni, S. R. 1999, *ApJL*, **516**, L25
van Leeuwen, A. G. J., Kouwenhoven, M. L. A., Ramachandran, R.,
Rankin, J. M., & Stappers, B. W. 2002, *A&A*, **387**, 169
van Leeuwen, J., Kasian, L., Stairs, I. H., et al. 2015, *ApJ*, **798**, 118
Venkatraman Krishnan, V., Bailes, M., van Straten, W., et al. 2020, *Sci*,
367, 577
Wang, N., Manchester, R. N., & Johnston, S. 2007, *MNRAS*, **377**, 1383
- Weisberg, J. M. 1996, in ASP Conf. Ser. 105, IAU Colloq. 160: Pulsars:
Problems and Progress, ed. S. Johnston, M. A. Walker, & M. Bailes (San
Francisco, CA: ASP), 447
Weisberg, J. M., & Huang, Y. 2016, *ApJ*, **829**, 55
Weisberg, J. M., Nice, D. J., & Taylor, J. H. 2010, *ApJ*, **722**, 1030
Weltevrede, P., Johnston, S., & Espinoza, C. M. 2011, *MNRAS*, **411**, 1917
Yao, J. M., Manchester, R. N., & Wang, N. 2017, *ApJ*, **835**, 29
Zhu, W. W., Berndsen, A., Madsen, E. C., et al. 2014, *ApJ*, **781**, 117